12-2015

Kinetic and Thermodynamic Modeling of Long Term Phase Stability in Alloy 800H Subjected to LWR Core Conditions

Wayne Ethan Pratt
University of Tennessee - Knoxville, wpratt1@vols.utk.edu

To the Graduate Council:

I am submitting herewith a thesis written by Wayne Ethan Pratt entitled "Kinetic and Thermodynamic Modeling of Long Term Phase Stability in Alloy 800H Subjected to LWR Core Conditions." I have examined the final electronic copy of this thesis for form and content and recommend that it be accepted in partial fulfillment of the requirements for the degree of Master of Science, with a major in Materials Science and Engineering.

Steven J. Zinkle, Major Professor

We have read this thesis and recommend its acceptance:

Brian D. Wirth, Kurt E. Sickafus

Accepted for the Council:
Carolyn R. Hodges

Vice Provost and Dean of the Graduate School

(Original signatures are on file with official student records.)

Kinetic and Thermodynamic Modeling of Long Term Phase Stability in Alloy 800H Subjected to LWR Core Conditions

A Thesis Presented for the
Master of Science
Degree
The University of Tennessee, Knoxville

Wayne Ethan Pratt
December 2015

ACKNOWLEDGEMENTS

The author would like to thank Dr. Jae-Hyeok Shim and Dr. Brian Wirth for their help with this project. Without their guidance and aid the current work would not have been possible. The author would also like to thank Dr. Steven Zinkle for his assistance in research for Alloy 800H.

ABSTRACT

An in depth literature review of Incoloy Alloy 800H was conducted and presented to summarize the current understanding of microstructural evolution under irradiation and secondary phase precipitate stability. Due to a lack of radiation induced segregation (RIS) data for Alloy 800H, Isopleth sections varying Cr, Ni, Ti, and Si were generated from a computational thermodynamics approach using ThermoCalc and analyzed to compensate for knowledge related to radiation induced precipitates (RIP's). These isopleths were analyzed for a composition range based off previous knowledge of RIS tendencies in austenitic stainless steels. Analysis of four major binary phase diagrams and complex phase diagrams calculated through ThermoCalc and MatCalc were used to simulate the precipitation kinetics during the lifetime of Incoloy Alloy 800H used in a light water reactor (LWR) core setting. These aging simulations were then conducted using the MatCalc heat treatments tool with $M_{23}C_6$ [Chromium Carbide], Sigma, and Ni_3Ti [Gamma Prime] set as the precipitates of interest.

A discrepancy was found relating to the presence of sigma phase at low temperatures between ThermoCalc and MatCalc complex phase diagram calculations. Several minor phases were noted from the complex phase diagrams and isopleths for further research. Isopleth sections revealed that no major RIP's should form given the current assumption of RIS behavior. Simulations of precipitation kinetics predict a precipitate coarsening somewhere between 6-7 years of operation for $M_{23}C_6$ [Chromium Carbide] precipitates. This results in a decline in number density and an increase in precipitate size. Anticipated radiation induced segregation has very little effect on $M_{23}C_6$ [Chromium Carbide] precipitate size, however increasing RIS results in the formation of fewer $M_{23}C_6$ [Chromium Carbide] precipitates. Sigma phase is found to increase in amount and decrease in size as segregation increases until the number of precipitates reaches a maximum between 20.42 and 14.42 wt% Cr. At doses greater than this the density of sigma precipitates is expected to decrease while the size of precipitates is expected to remain consistent.

TABLE OF CONTENTS

LIST OF TABLES

LIST OF FIGURES

CHAPTER I

INTRODUCTION AND GENERAL INFORMATION

1.1 Introduction

Recent studies have considered Incoloy alloy 800H as a candidate for structural material applications in Gen IV nuclear reactor systems [1]. Due to its high Ni and Cr content, Alloy 800H has a high corrosion resistance, strength at high temperatures, resistance to void swelling, and ability to retain most of its properties at high temperatures [1-4].

Alloy 800H has been studied for use in nuclear systems since the early 1950's. It was approved by the American Society of Mechanical Engineers (ASME) Boiler and Pressure Vessel (BPV) Code Committee in 1963 for use in nuclear reactor technology. Since its approval, studies have focused on determining its effectiveness in heat exchanger technology for use in some current, as well as Gen IV, nuclear power systems. Currently, it is mostly used commercially for furnace components and equipment, petrochemical furnace cracker tubes, reheater tubing, sheathing for electrical heating elements, and many other applications [1, 2, 5].

One possible use being considered is for the very high-temperature reactor (VHTR) design. The VHTR is expected to produce a highly corrosive environment which will require materials with good corrosion properties. The

VHTR design is envisioned to be a thermal neutron spectrum reactor with helium coolant at temperatures up to 950˚C and pressures up to 7MPa for a lifetime of 60 years. Alloy 800H is being considered here as an alternate candidate material for alloys 617 and 230 in applications such as the compact heat exchanger, tubular helical coil, and other types of heat exchangers [1].

Many studies have been conducted to investigate mechanical and corrosion properties of Alloy 800H. More recent studies investigated its properties under radiation. In this work, we attempt to create a predictive model to evaluate the second phase precipitates during operation in the core of a light water reactor. To do this we will use computational thermodynamic CALPHAD type databases to investigate the thermodynamic properties of Alloy 800H. After some investigation we will then attempt to simulate precipitate kinetics by modeling the heat treatment this material will undergo in core settings for 100 years. We will study the long term phase stability under these settings, modifying the composition of the material simulated to account for grain boundary segregation under irradiation.

1.2 Objectives of Study

The focus of this project is to model the long term phase stability of Incoloy Alloy 800H under core conditions. Study of phase stability will be conducted through the CALPHAD method, coupling thermodynamic and diffusion based databases to model phase stability. A careful look of the thermodynamic properties of Alloy 800H will be performed with ThermoCalc modeling. In order

to investigate the long term phase stability, the information gathered will then be utilized to run simulations of precipitation kinetics for the lifetime of Alloy 800H when used in a core setting. These simulations will utilize the coupling of thermodynamic and diffusion databases in MatCalc. The final results will be analyzed to help determine the anticipated second phase precipitate stability of Alloy 800H as a result of assumed radiation induced segregation in reactor settings.

1.3 Limitations of Study

Several methods have been utilized to improve the service lifetime and properties of Alloy 800H. One such method utilized grain boundary engineering (GBE) through processes of cold working and thermal annealing post solution anneal. These thermos-mechanical treatments (TMT) were very successful for improving the thermal properties of Alloy 800H [2, 6-8]. Laser surface alloying (LSA) was also utilized to study modified surface properties of Alloy 800H [9]. Although these studies make considerable improvements to the material properties of Alloy 800H, they are incompatible with the simulation methods chosen for this project. They will therefore be summarized and discussed only.

CHAPTER II

LITERATURE REVIEW

2.1 Introduction

Studies on the Incoloy 800 series have been conducted since their introduction to the market in the 1950's. In 1963 Alloy 800H was approved by the ASME Boiler and Pressure Vessel Committee and the design stresses were published in Code Case 1325. Alloy 800H, initially named Alloy 800 Grade 2, requires a carbon concentration to be within the range of 0.05 to 0.10 wt% with an average grain size of ASTM 5 or coarser (>65μm) [4]. Due to its good corrosion resistance, strength at high temperatures, resistance to void swelling, and ability to retain most of its properties at high temperatures, Alloy 800H is being considered for several next gen nuclear models such as the very high temperature reactor (VHTR), the gas-cooled fast reactor (GFR), the super critical water reactor (SCWR), and the lead-cooled fast reactor (LFR) [1-4, 10-12]. Alloy 800H was even considered for the Prometheus Space Reactor System [13]. It is widely used in the petrochemical industry, in addition to applications such as furnace components, reheater tubing, and sheathing for electrical heating elements [1, 2, 5], and is currently being considered for several high temperature designs such as heat exchangers and heating coils [1, 5].

Unfortunately there is very limited radiation data on Alloy 800H. Particularly, there is little to no information about radiation induced segregation

(RIS) in Alloy 800H. Alloy 800H is noted as an austenitic material and is similar enough in composition to austenitic stainless steels that this data could be assumed to be similar. This is convenient since RIS in austenitic steels has been widely studied. Previous phase stability modeling was conducted by Shim for 316 stainless steel [14]. In this study, Shim determined the extent of RIS at 0-20 dpa for 316 steel through a comprehensive literature search. This data was then expressed as compositional changes at grain boundaries and sinks to use in his simulations. These same data should be similar enough to the actual RIS data for Alloy 800H that it can be used in our study.

2.2 Properties of 800H

Figure 24-Figure 26 in the Appendix show the alloying compositions, physical constants, and modulus data provided by Special Metals Corporation [4]. Special Metals Corporation also summarizes thermal and electrical properties, tensile properties, fatigue strength, creep and rupture properties, and some processing methods for Alloys 800, 800H, and 800H. Due to having the same composition, all three alloys exhibit similar properties at moderate temperatures. Among these shared properties are high a resistance to corrosives such as oxides, carbides, sulfides, and nitrides. This corrosive resistance comes from the high Ni and Cr concentrations in the Alloy 800 series. Due to these alloying elements, it is also found that the two most common precipitates to nucleate within this series are ɣ' (Ni_3Ti) and $M_{23}C_6$ ($Cr_{23}C_6$). Optimization of ɣ' precipitation is known to have positive effects on the rupture

stress lifetime of the material [15]. Alloys 800H and 800HT exhibit superior creep and rupture strength in high temperature environments over extended periods of time. It should be noted that Alloy 800 exhibits superior mechanical properties at room temperature, however this alloy loses those properties much more rapidly than its counterparts when exposed to high temperatures for long periods of time [4]. It should also be noted that the tensile properties of Incoloy Alloy 800H is not superior to the tensile properties of other modern alloys including Alloy 617 [16].

2.3 Thermomechanical Treatment

Tan and Allen published a paper in 2005 studying the aspects of grain-boundary engineering (GBE) in Incoloy Alloy 800H [9]. GBE was initially proposed by Wantanabe in the early 1980's to improve material properties like strength, ductility, creep, weldability, and corrosion resistances [6]. The idea behind GBE is to increase the amount of low-Σ grains produced within the material through the use of a thermo-mechanical treatment (TMT). This treatment process would cause grains to grow with a high density of coincident sites. The goal in particular is to grow more Σ3 grain boundaries to produce less stress within the material.

Tan proposed a TMT process for Alloy 800H in which the material was cold worked to 6.6% deformation followed by an annealing at 1050˚C. In his experiments he used a scanning electron microscope (SEM) with electron backscattered diffraction (EBSD) to look at the types of grains found. The results, displayed in Figure 1 depicted the production of low Σ grain boundaries

was increased when the material was annealed prior to the cold working. In addition the production of Σ3 grain boundaries was improved the most during the 90 minute anneal [9]. This process is later used for further studies which found improved corrosion resistance and mechanical strength as well as reducing the formation of radiation induced precipitates (RIP's) and voids produced from neutron radiation, thus improving radiation resistance [6, 8, 17-21].

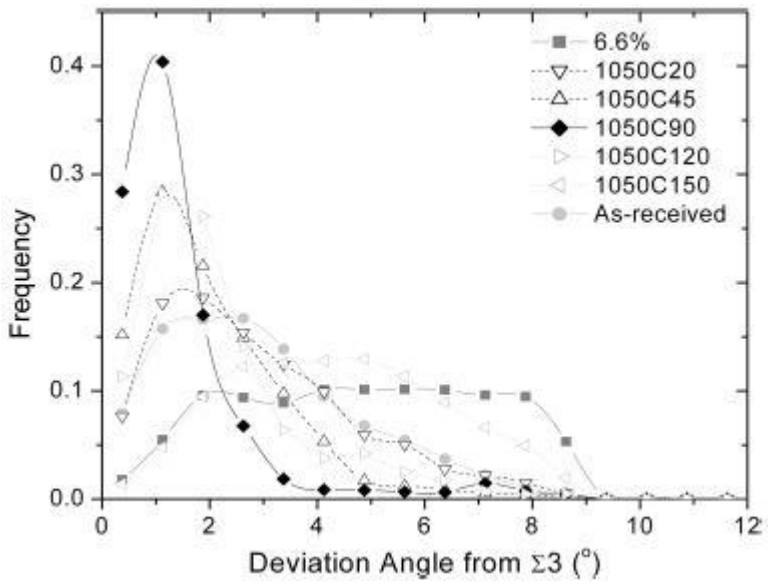

Figure 1-Image from Tan and Allen showing the deviation of coincident site lattice boundaries from the Σ3 structure based on different TMT annealing times. In the image the "6.6%" line represents 6.6% cold working with no following heat treatment [9]

2.4 Laser Surface Alloying

Laser surface alloying was investigated in the 1990's as a possible method of improving material surface properties of Alloy 800H. The goal was to

improve material lifetime, namely in corrosive environments. Aluminum powder was liquefied and fed onto the surface of Alloy 800H samples at the contact point of a 5000kW CO_2 continuous wave laser with a beam spot area of 64mm^2. The aluminum seemed to bond with the surface of the alloy and some phase analysis was conducted. Their results, however were inconclusive and did not actually test for corrosion resistance [7, 22].

2.5 Structure and Microstructure

Incoloy Alloy 800H is an austenitic material with an FCC structure. Special Metals denotes common precipitates as titanium nitrides, titanium carbides, and chromium carbides. Among these precipitates, the nitrides are stable at all temperatures below the melting point. The chromium carbides are noted to precipitate between 540 and 1095˚C [4]. In addition, Tan et al. determined through x-ray diffraction that the crystal structure is cubic in nature with a=3.593Å belonging to the spacegroup Fm3m [9].

In 1985, in response to the addition of Alloy 800H to the ASME Code (Case N-47), Nilsson and Thorvaldsson investigated the microstructural changes caused by ageing in Alloy 800H to better understand its fatigue properties. The ɣ’ phase is a common precipitate in Alloy 800H at moderate to high temperatures (550-650˚C). Precipitation of ɣ’ has been shown to benefit fatigue resistance. Observable precipitates are not observed in the solution annealed material. Prior to ageing in the range of 550˚C and 650˚C for 1000 hours, $M_{23}C_6$ and ɣ’ are found to nucleate as shown in Figure 2. $M_{23}C_6$ (the larger precipitate in Figure 2)

is found to nucleate primarily at grain boundaries, although it has a slight tendency to nucleate at dislocation sights intragranularly. High density precipitation of smaller ɣ' appears to occur at intergranular dislocations only. It has also been noted that ageing can cause a strong grain size effect that leads to inhomogeneous deformation [23].

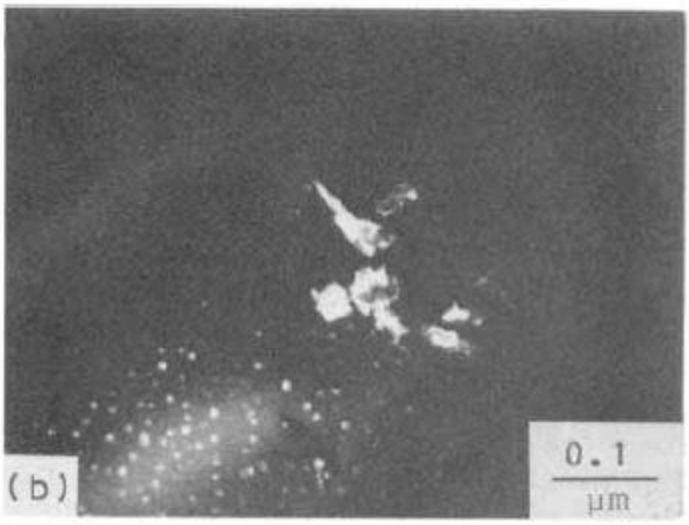

Figure 2-Image provided by Nilsson and Thorvaldsson showing a dark field micrograph of large M23C6 and the smaller, more dispersed ɣ' precipitates following aging and fatigue testing [24]

Later study of TMT samples by Tan et al. (using the same TMT procedure recommended by Tan and Allen described above) reinforced the results of Nilsson and Thorvaldsson. The presence of $M_{23}C_6$ and ɣ' was confirmed in both samples with and without TMT. Neutron irradiation studies found that at low doses (1.3-3 dpa) the size of ɣ' precipitates is reduced while the density is increased. For $M_{23}C_6$, the size and density were both reduced. It is suggested that at high radiation damage levels, $M_{23}C_6$ particles are dissolved back into the

matrix. In addition to precipitate nucleation and growth, Tan et al. noted that radiation hardening was greatly influenced by precipitate behavior. Specifically $M_{23}C_6$ showed the greatest effect on hardening. As the material is aged in these precipitates are expected to grow. This growth in turn is expected to raise material hardness and cause embrittlement. Tan et al. found that with increasing radiation dose, $M_{23}C_6$ precipitates actually dissolved back into the matrix, reduced material hardness by 14.6%. In addition, the TMT samples were found to have a reduced hardness of 40.9% from the solution annealed samples [8].

In addition to $M_{23}C_6$ and ɣ' precipitates, Cao et al. found the presence of Ti(C,N) precipitates in Alloy 800H samples aged for 50 hours at 750˚C. During the aging experiments Cao did not report any ɣ' precipitates, however Cao did confirm $M_{23}C_6$ as being predominantly $Cr_{23}C_6$. The formation of $Cr_{23}C_6$, especially under radiation, is likely due to chromium and carbon migration to grain boundaries. Figure 3, reproduced from Cao et al. shows the migration of Cr, C, Ti, and Ni prior to deformation by compression. Both carbon and chromium can be observed to migrate towards grain boundaries, while carbon also migrates towards what could be a TiC rich precipitate. Cao also noted that $M_{23}C_6$ did not form in Σ3 grain boundaries, reinforcing the findings of Tan et al [2].

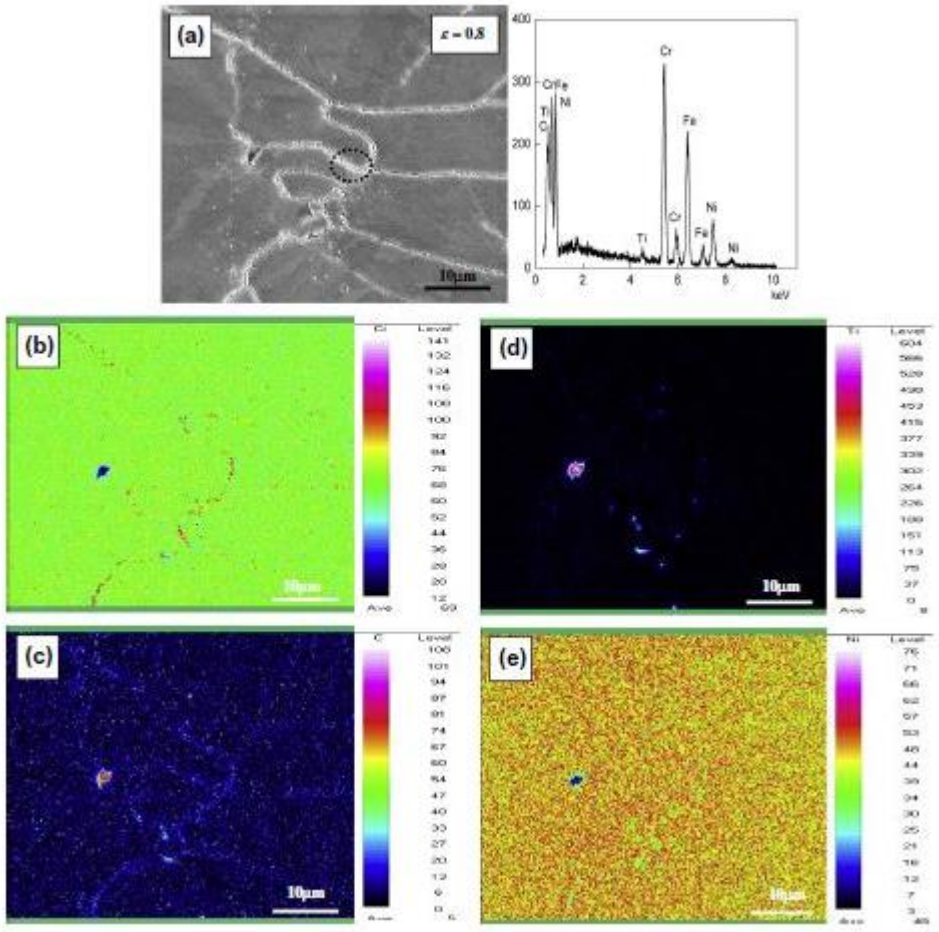

Figure 3-Electron probe microanalyzer (EPMA) results of Alloy 800H samples that were aged to 750˚C for 50 hours provided by Cao et al. [2]

Both Gan and Tan investigated the radiation-induced production of faulted loops as well. Faulted loops are an important mechanism for radiation hardening in austenitic stainless steels. Gan's irradiation studies with Ni irradiations found that at high doses, the amount of dislocation loops increased from $(1.2 \pm 0.2) \cdot 10^{16}$ cm^{-3} (at 5 dpa irradiations) to $(2.3 \pm 0.4) \cdot 10^{16}$ cm^{-3} (at 50 dpa irradiations) while the size decreased from 12.5 ± 0.2 nm to 8.4 ± 0.2 nm. Gan described the irradiated microstructure as dominated by faulted loops [3]. Tan recorded the sizes of Frank loops in Table 1 [8]. Based off Tan's results, the dislocation loop density is increased dramatically when considering neutron radiation instead of heavy ions. This density can be slightly reduced by TMT, however this does not mitigate enough of the loop production to equate it to the heavy ion results. Dislocation loop size is also significantly reduced when comparing neutron irradiation to heavy ion irradiation.

Table 1-Record of size, density, and hardening properties for some defects and precipitates in Alloy 800H after neutron irradiation at 500˚C to 1.3 and 3 dpa provided by Tan et al. [8]. The bracketed numbers represent values for samples that were given a TMT which included a 6.6% cold working followed by annealing at 1050˚C for 1.5 hours and water quenched prior to irradiation.

RIF's	Dose (dpa)	Sized (nm)	Density N (x1022 m^{-3})	Hardening $\Delta\sigma_y$ (MPa)
Frank Loops	1.3 3	n/a 6.0 {5.7}	n/a 2.85 {2.11}	n/a 40 {31}
Voids	1.3 3	3.6 3.1 {4.0}	0.025 1.9 {0.12}	1 16 {3}
$M_{23}C_6$	1.3 3	34.2 5.4 {n/a}	0.055 n/a {n/a}	248 n/a {n/a}
ɣ'	1.3 3	34.7 2.2 {2.3}	0.034 1.46 {0.49}	197 325 {191}

2.6 Dynamic Recrystallization

Brunger, Wang, and Gottstein published several papers on dynamic recrystallization (DRX) in the late 1900's. Their analysis utilized compression at high temperatures followed by He gas quenching (80K/s) to introduce dislocations into the samples. Afterwards the specimens were examined by TEM and EBSD (SEM). They found that DRX by bulging only occurred at low strains and was not the primary nucleation mechanism, however DRX was also found to occur at both low and high strains. After further investigation twinning was found to be the most likely cause of DRX at high strains (and low strains in addition to bulging). The generation of twins in single crystals is suggested to be triggered by dislocation interactions in the subgrain boundary. Brunger et al. found that the fraction of twins found at the interface between initial grains and DRX grains was more than 20%. Although they concluded twinning as the greatest contribution to DRX, a complete understanding of this was still unknown [25]. Further study by Wang et al. found that the preferential nucleation sites for DRX were the initial grain boundaries due to the orientation gradients between the grain boundaries. This was believed to occur through the growth of dense dislocation walls (DDW's) which would then be consumed by moving grain boundary walls [25].

Later experiments by Cao confirmed earlier research that formation of carbides (such as $M_{23}C_6$) lead to pinning of grain boundaries. This pinning effect kept DDW's from being dissolved and thus prohibited the process of DRX [23, 26-28]. Due to this Cao observed no DRX in any aging experiments because of

the increase in $M_{23}C_6$ precipitates formed during aging [2]. It should also be noted that the aging temperature for specimens in these experiments was 750˚C. In addition, the precipitation of $M_{23}C_6$ can be greatly reduced through the use of TMT.

2.7 CALPHAD Method

The CALPHAD Method was originally an acronym for the “calculation of phase diagrams.” The overarching goal of CALPHAD is to couple computational methods with thermochemical data. The origin of CALPHAD begins with Van Laar’s applications of Gibbs free energy concepts to phase equilibria in 1908. This application was however not widely considered until the 1950’s due to the prevalence of other theories and the lack of computational power required to carry out the calculations to the required extent. Once qualitative results were successfully presented, the scientific community began to work together on research. Efforts to help characterize steel began using rudimentary polynomial descriptions of the thermodynamic properties of iron. Communities began to generate databases, which required many different values to be documented including lattice stabilities (including stabilities for structures that were unstable enough that they could not be produced via experiment), interaction parameters between elements and species within the system, and Gibbs free energy values. Kaufman, in 1967, presented the first work demonstrating the power of the CALPHAD approach [29]. In lieu of the potential for the model proposed, Kaufman’s work did not really begin to even be accepted until the publication of

the first CALPHAD based text book in 1970. Even with the addition of this text CALPHAD did not begin to gain much recognition until Kaufman was able to arrange the first CALPHAD meeting in Boston (1973) to discuss developing a uniform description of phases to create an international system of interchanging data as well as discussing the details behind phase boundary calculations. As per Kaufman's initial suggestion, a second meeting was held in Grenoble (1974) to compare results from the past year gathered by the different groups as well as planning future meetings. These meetings continued in subsequent years as CALPHAD began to become a useful tool for scientists. In the late 1970's and 1980's, CALPHAD began to gain much more attention with both the publication of its very own journal and the aid of conferences on phase diagrams and thermodynamics [29].

CHAPTER III

METHODS

3.1 Overview

In order to address the problem of phase stability a series of thermodynamic and diffusion based modeling was chosen. Initial thermodynamic modeling was conducted with the ThermoCalc software, calculating complex Phase Diagrams and Isopleths to help predict phase formation and changes both within the grains and along grain boundaries due to RIS. MatCalc software was then employed to help further investigate phase status by running stepped equilibrium point checks to determine phase amount and composition at varying temperature. Once an understanding of phase status was obtained a compositional adjustment was made based off of the research of Shim [14]. Finally simulations of precipitation kinetics were performed using MatCalc for assumed compositions reflecting RIS at 0, 5, 10, and 20 dpa neutron irradiation damage to simulate the lifetime of Alloy 800H.

3.2 CALPHAD Method

An important feature of our work lies in the modeling programs. These two programs utilize CALPHAD based databases which allow for the calculation of complex phase diagrams for modeling use. CALPHAD employs a rigorous

algorithm that utilizes the knowledge of lower order phase diagrams such as binary phase diagrams to extrapolate higher order systems [29].

CALPHAD methodology utilizes knowledge of Gibbs free energy to calculate thermodynamics and system equilibria. CALPHAD based databases were constructed through the collaboration of many different scientific communities who contributed experimentally determined values for chemical potential, enthalpies, entropies, lattice stabilities, interaction parameters, and other factors to help build and support Gibbs free energy curves. CALPHAD type models then solve to reduce the Gibbs free energy of the known system to calculate for simple and complex equilibria by first looking at the Gibbs energy of each component by

$$G = \sum_i n_i \bar{G}_i \tag{1}$$

where n_i and $\bar{G}_i$ are the amount and activity of component i respectfully, or by considering the phases through the use of

$$G = \sum_{\phi} N^{\phi} G_m^{\phi} \tag{2}$$

where N^{ϕ} and G_m^{ϕ} are the amount and Gibbs energy for phase ϕ. Analysis for simple binary phase diagrams is conducted by taking these curves and setting them equal to each other for each pair combination of phases. For instance, in an iron-carbon binary phase diagram, one can map the boundary between the austenite (ɣ) and liquidus (liquid + ɣ) phase regions by setting the related Gibbs functions (pertaining to a common component, A) equal to each other

$$\bar{G}_A^{\gamma} = G_A^{\gamma \to liq} \tag{3}$$

where

$$\bar{G}_A^{\gamma} = RT \log_e x_A \tag{4}$$

for an ideal solution and $G_A^{\gamma \to liq}$ is the Gibbs energy of the fusion of solid component A with respect to ɣ. Solving this equation for combinations of temperature and composition that make the statement true then produces the phase boundary.

Another way of computing this is through the definition of Gibbs free energy

$$\Delta G = H - T\Delta S \tag{4}$$

where H is the Enthalpy and S is the Entropy of the system. By employing this system equation (3) becomes

$$\bar{H}_A^{\gamma} - T\bar{S}_A^{\gamma} = H_A^{\gamma \to liq} - TS_A^{\gamma \to liq} \tag{5}$$

which can then be solved as

$$T = \frac{\bar{H}_A^{\gamma} - H_A^{\gamma \to liq}}{\bar{S}_A^{\gamma} - S_A^{\gamma \to liq}} \tag{6}$$

In order to solve this equation using temperature dependent enthalpy and entropies, as is the case in most real solid solutions, CALPHAD type programs use an iterative process with a varying temperature which uses

$$\Delta G^{l\phi} = \sum_i x_i^{\phi} \bar{G}_i^{liq} - G^{\phi} \tag{7}$$

where $\Delta G^{l\phi}$ is the change in Gibbs energy of compound ϕ, x_i^{ϕ} is the mole fraction of component i in compound ϕ, $\bar{G}_i^{liq}$ is the partial Gibbs energy of i in the liquid, and G^{ϕ} is the Gibbs energy in compound ϕ. The programs supposes an initial value for the temperature, which is chosen by the user, and begins to step the temperature in a direction that reduces the value of $\Delta G^{l\phi}$ until it reaches a value which is below a defined accuracy limit which is sufficiently small enough. For more rapid calculations the program utilizes the Newton-Raphson method.

In addition to binary and ternary calculations, CALPHAD allows for the development of computational modeling programs like ThermoCalc and MatCalc to create models for higher order systems. These models are extrapolated from the data of related binary and ternary systems by the programs. It should be noted that these models are still under development and can have a degree of variance resulting from differences in recorded data, quality of data recorded, accuracy of the program used, and the program version. These errors can be minimized by rigorous calculation and comparison to experimental data, however calculations will always be limited by the amount and quality of data in each database. Thus for our project it was important to choose updated databases

which would best reflect our material. We have chosen to use ThermoCalc's SSOL5 database to run all calculations in ThermoCalc (software version 3.1). Two MatCalc (software version 5.60) databases were explored to determine the database which best matches with our material. These databases were 'mc_fe' (version 2.023) and 'mc_ni' (version 2.012). A modified copy of each MatCalc database was also used which included updated RIS data used by Shim in his modeling for 316 stainless steels [14].

3.3 Binary and Complex Phase Diagrams

Initially, ThermoCalc was used to calculate the Alloy 800H complex phase diagram for understanding the relationships between phases in Alloy 800H. Expected phases are γ' and $M_{23}C_6$ from the literature. The carbide phase of Ti(C,N) has also been reported in the literature after an intensive aging heat treatment at high temperature (750˚C), however it is not expected to be found in our simulations. In addition to searching the literature, binary phase diagrams were calculated to help set up calculations for the complex phase diagram. These were mapped using the binary tool in ThermoCalc and compared to binary phase diagrams calculated by Computational Thermodynamics Inc. (which are published online at calphad.com) to ensure the accuracy of these graphs. The decision to re-calculate these in ThermoCalc instead of simply referencing the graphs generated by Computational Thermodynamics was made due to the fact it was pertinent to be able to examine the phase diagram at all temperatures between room temperature and 1177˚C. The binary diagrams provided by

Computational Thermodynamics do not examine phase stability below 600˚C. Phase diagrams were also calculated using MatCalc to determine any differences between the two programs and, by comparison, between the two databases. All phase diagrams and equilibrium calculations were conducted using the composition provided by Gan et al. in Table 2 [3]. Due to being impurity elements, phosphorus and sulfur were left out of simulations to focus only on important precipitates. Mn, Si, and Cu were kept in calculations despite also being impurity elements due to being larger contributors to the material as impurity elements.

Table 2-Composition of Alloy 800H samples used by Gan et al. in 2006 for heavy-ion irradiation

Fe	C	Mn	P	S	Si	Ni	Cr	Ti	Cu	Al
Balance	0.069	0.76	0.014	0.001	0.13	31.59	20.42	0.57	0.42	0.50

For ThermoCalc simulations, two options were available for simulating phase diagrams, a command log mode and a graphical mode. Initial versions of ThermoCalc run only through the command log, however the updated software now also includes a user interface setting. While this setting might be easier to use, it does not include all of the features that ThermoCalc offers. In addition it still has some bugs that limit its graphical functions and reduce the speed of data analysis. Due to these issues, we have chosen to use the command setting in the updated software for calculating complex phase diagrams. The binary phase

diagrams, however were calculated using the graphical interface since the binary tool did not face any of these challenges.

Computational Thermodynamics Inc. publishes CALPHAD based binary phase diagrams online for public use. Binary phase diagrams of Fe-C, Fe-Cr, Fe-Ni, and Ni-Cr were used to help set up ThermoCalc calculations. We reproduced these phase diagrams in Figure 4 using ThermoCalc's binary phase diagram calculator to show the four major binary phase diagrams for Alloy 800H. Based off the graphs in Figure 4, immiscible phase regions (regions with more than one phase) for our material could occur between many phases including austenite, ferrite, cementite, sigma, FCC(Ni), FCC(Cr), BCC(Fe), BCC(Cr), and $FeNi_3$ as well as including several liquidous phases at higher temperatures. Due to these observations, miscibility gap checks were run for all FCC and BCC phases as well as sigma phase and the liquid phase in all ThermoCalc calculations.

Phase diagrams were calculated in ThermoCalc through the use of the Define Diagram (def-dia command) mode in the Poly module. This mode calculates a diagram given a set of variables defined by the user. In our calculations we will vary temperature and request the mass fraction of each phase to be plotted. After launching def-dia the database, SSOL5, and composition of each element, with iron as the major constituent, given in Table 3 were entered into the Poly module. This module is used to set up the initial conditions for the calculation.

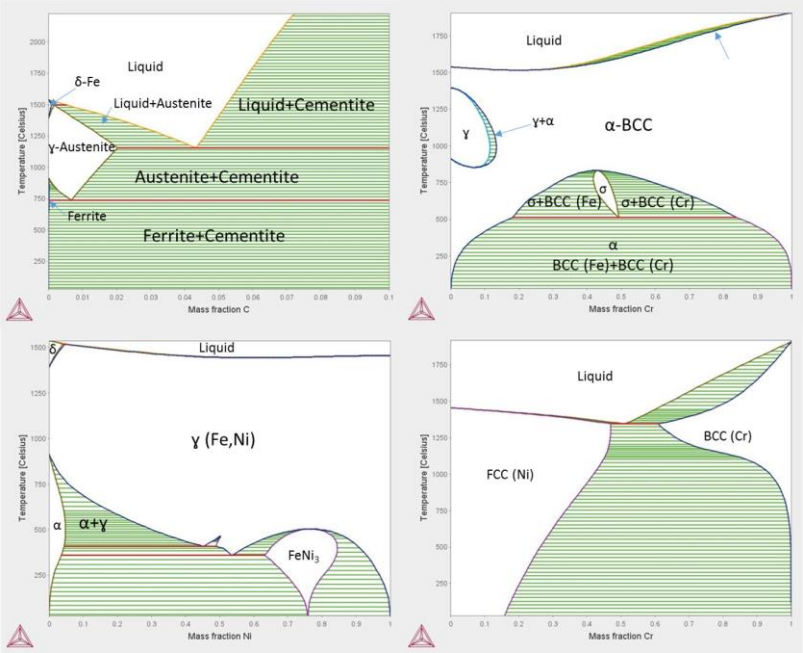

Figure 4-Binary phase diagrams calculated with ThermoCalc.

After accepting the database for lookup and the compositions poly then asks a series of questions. The initial temperature was set at 1000˚C. This temperature acts only as a launching point for the stepped calculation and does not necessarily reflect the temperature or phase regime we are most interested in. Prior to setting the initial temperature the program was told not to add or remove any phases. Poly then requests phases for miscibility gap checks. The phases “SIGMA”, “BCC_B2”, “FCC_L12”, “FCC_L10”, and “FCC_A1” were designated for miscibility gap checks while keeping the elements contained in each phase set to default. The Poly module then processed the data and then asked for

some boundary conditions. The temperature was varied from 200˚C to 1700˚C with a step size of 25˚C and the second axis, which will be our output, was set to be the mass fraction of all phases. Finally, the phase diagram was calculated. The results from this calculation can be found in the next chapter.

The equivalent MatCalc phase diagrams were calculated based off of the same initial alloying conditions found in Table 3. Due to previous research, our group was in the possession of two useful thermodynamic MatCalc databases initially. The iron database 'mc_fe' (version 2.023) and nickel database 'mc_ni' (version 2.012) were both assessed to determine which database was better suited for our material. In addition, two modified databases, 'mc_fe' (version 2.003) and 'mc_ni' (version 2.011) were also assessed. The modified iron thermodynamic database was created by Dr. Shim to incorporate RIS behavior in 316 stainless steel [14]. This database was created from the version 2.023 iron database. A copy of the nickel database (version 2.012) was created and adjusted with the same data to reflect the changes Shim made to the iron database. This modified nickel database was labeled 'mc_ni' (version 2.011). These modifications include the addition of data for the Ni_3Ti precipitate phase that forms as a result of radiation induced segregation in stainless steels. It should be noted that this phase does not normally appear in austenitic stainless steels and is a radiation induced precipitate. It is, however a common precipitate in high nickel alloys under normal conditions. Thus, data for this phase was already included in the nickel database. To distinguish between the two phases,

the original data in the nickel database was left labeled as GAMMA_PRIME. The new data included in the modifications was labeled as Ni_3Ti. The modifications also included adding data for G_Phase, which was also already included in the database.

In order to prepare for simulations of precipitation kinetics during anticipated operating conditions, it was imperative to not only determine which databases to use, but also to limit the amount of phase data utilized by the calculation. In order to limit the calculation to only the necessary phases, four sets of phases were devised to investigate how removing phases from the calculation would change the programs ability to construct a phase diagram. These sets were defined as the following:

- Set 1-Only the phases reported by the phase diagram calculated through ThermoCalc
- Set 2-Suggested phases reported in the works of Dr. Shim
- Set 3-Phases known to be present in austenitic stainless steels
- Set 4-All phases recorded within the chosen MatCalc thermodynamic database

Each simulation was set up to run from an equilibrium launching point of 400˚C. To produce the phase diagrams, temperature step equilibriums were set to run within the range of 100˚C and 2000˚C with a step interval of 5˚C. Plots

were then generated plotting the phase fraction versus the temperature. The phase diagrams produced will be discussed in the next chapter.

3.4 Isopleths and Compositional Analysis

The construction of isopleth plots generates a graph similar to a binary phase diagram in appearance. This feature of ThermoCalc generates a phase diagram for a given composition, however it varies a single element from 0 wt% to 100 wt%. This feature allows for observation of the material when a specific element is removed or added to the system in a homogeneous manner. Isopleth graphs can also be used for looking at issues of segregation where a specific component tends to either migrate towards or away from an area of interest. For these studies, isopleth calculations were carried out to help examine the effects of compositional shifts caused by RIS in Alloy 800H. By reproducing isopleth regions we can evaluate the possible effects of RIS on phase nucleation without experimentally investigating them.

To calculate isopleth regions we decided that the thermodynamic databases of ThermoCalc would be sufficient. Isopleths were calculated using the command mode in the ThermoCalc software through the Poly module. With the SSOL5 database previously mentioned, the material was defined with base element iron and the composition given in Table 3. The starting temperature this time was set at 2000˚C to avoid convergence issues and the miscibility gap check was set for the same phases that were used in calculating the ThermoCalc phase diagrams. Finally, mapping was conducted for Cr, Ni, Si, and Ti. The

extent of mapping for each element varied on the composition of that element in Alloy 800H. Mapping was conducted from 200˚C to 2000˚C at 25˚C step intervals. The final plots will be discussed in the next chapter.

It is important to remember that the focus of this study is to investigate the phase stability of Alloy 800H which could result from radiation induced segregation. The models chosen do not have the capability to incorporate effects from radiation. As a result, these effects must be accounted for in other ways. In a reactor, radiation effects occur simultaneously with thermodynamic effects and diffusional effects in a material. Since these programs are unable to account for all three effects, we will account for segregation effects manually before running each precipitate kinetics simulation. Doing this makes the assumption that the material is irradiated, then heated instead of being irradiated and heated simultaneously. In order to do this an in-depth study was taken into radiation induced effects, namely RIS, in alloy 800H. Unfortunately, not much RIS literature exists for Alloy 800H. Thus, a detailed look at RIS in austenitic stainless steels was also utilized. The use of RIS data from steels can be justified through both materials being austenitic, FCC, and iron based however this will also add a small degree of inaccuracy to our study.

After an intensive phase analysis, studies on RIS in Alloy 800H and austenitic stainless steels, and investigations into isopleth regions for select RIS elements; compositional adjustments were made to predict the effects of RIS on grain boundary composition based off the works of Shim [14]. It was decided to

use similar composition shifts to those used by Shim in his work with 316 steel due to the similarities in material structure and phase production. The compositions determined for each dose can be found in Table 3. These will be used for precipitate kinetics calculations in MatCalc.

Table 3-Compositions invented to reflect radiation damage in Alloy 800H for use in MatCalc precipitate kinetics simulations (wt%)

	Fe	Cr	Ni	Al	Mn	Si	Ti	C	Cu
800H	Balance	20.42	31.59	0.5	0.76	0.13	0.57	0.069	0.42
Segregation At 5 dpa	Balance	17.42	36.59	0.8	0.26	2.53	0.87	0.069	0.42
Segregation At 10 dpa	Balance	15.42	39.59	0.8	0.26	4.53	0.87	0.069	0.42
Segregation At 10 dpa	Balance	14.42	42.59	0.8	0.26	4.53	0.87	0.069	0.42

3.5 Simulations of Precipitate Kinetics

After a thorough thermodynamic analysis of Alloy 800H select phases were determined as possible precipitates. Simulations of precipitation kinetics were performed focusing on these phases in order to look at the long term phase stability of Alloy 800H. To set up these simulations the thermodynamic database selected by the results from the complex phase diagram analysis (See Section 4.1) was used in conjunction with a nickel diffusional database ‘mc_ni’ (version 2.004). Four simulations utilizing the compositions assumed for 0, 5, 10, and 20

dpa neutron damage were run to represent 100 years of operation in a LWR core. An initial solution anneal was also included. To program this simulation of precipitation kinetics the software was told to ramp up the temperature from 25˚C to 1177˚C in 30 minutes, hold for 2.25 hours, and then cool (quench) in 5 seconds back to 25˚C. Then the simulation was told to ramp up the temperature to 400˚C in 30 minutes and hold for 100 years.

It was decided from the phase analysis to focus on $M_{23}C_6$, Sigma, and γ' (Ni_3Ti) as possible precipitate phases. Austenite was set as the matrix phase with the grain size set to the minimum limit (65μm) as required by the material's standard [4]. In addition, mechanical properties such as Young's Modulus, Poisson's ratio, and basic strength were set according to the parameters found in the Special Metals specification. For simple calculation of Young's Modulus, see Figure 27 in the Appendix. Precipitates for γ'(Ni_3Ti), Sigma, and $M_{23}C_6$ were created in the Phase Status window. From the works of Nilsson and Tan γ' precipitates are known to nucleate intragranularly in Alloy 800H, typically at temperatures of 550-650˚C although neutron radiation has been known to lower this temperature regime [16, 24]. For this reason γ' was set to nucleate at dislocation sites only. $M_{23}C_6$ is known to commonly precipitate at grain boundaries, however there has been some report of nucleation intragranularly at dislocations. The nucleation of sigma is known to occur at dislocations in austenitic stainless steels, however is presently unknown for Alloy 800H. The

aging simulations were calculated through the precipitate kinetics command with a maximal T-step of 10, the results of which are presented in the next chapter.

CHAPTER IV

RESULTS AND DISCUSSION

4.1 Phase Analysis

Figure 5 was calculated with ThermoCalc by using the composition from Table 3. Unfortunately, the software was not able to resolve the phase diagram to include lower temperatures, however it was able to include most of the areas of interest. It should also be noted that the database used for these calculations was ThermoCalc's SSOL5 solid solutions database, which will differ from the MatCalc Fe and Ni databases used later. This figure shows a dominant matrix structure of Austenite up until around 1300˚C when it begins to melt, which is in agreement with material data presented by Special Metals Corporation. Notable minor phases produced are several BCC phases, a minor Ni-based FCC phase, Sigma phase, ɣ' (NI_3TI), and $M_{23}C_6$ ($Cr_{23}C_6$). The sigma phase forms notably at temperatures above 400˚C in the ThermoCalc simulation. All other phases are expected to be present at 400˚C based on the TermoCalc simulation.

Upon analysis of the ThermoCalc complex phase diagram, the selected sets for MatCalc calculations were defined as the following:

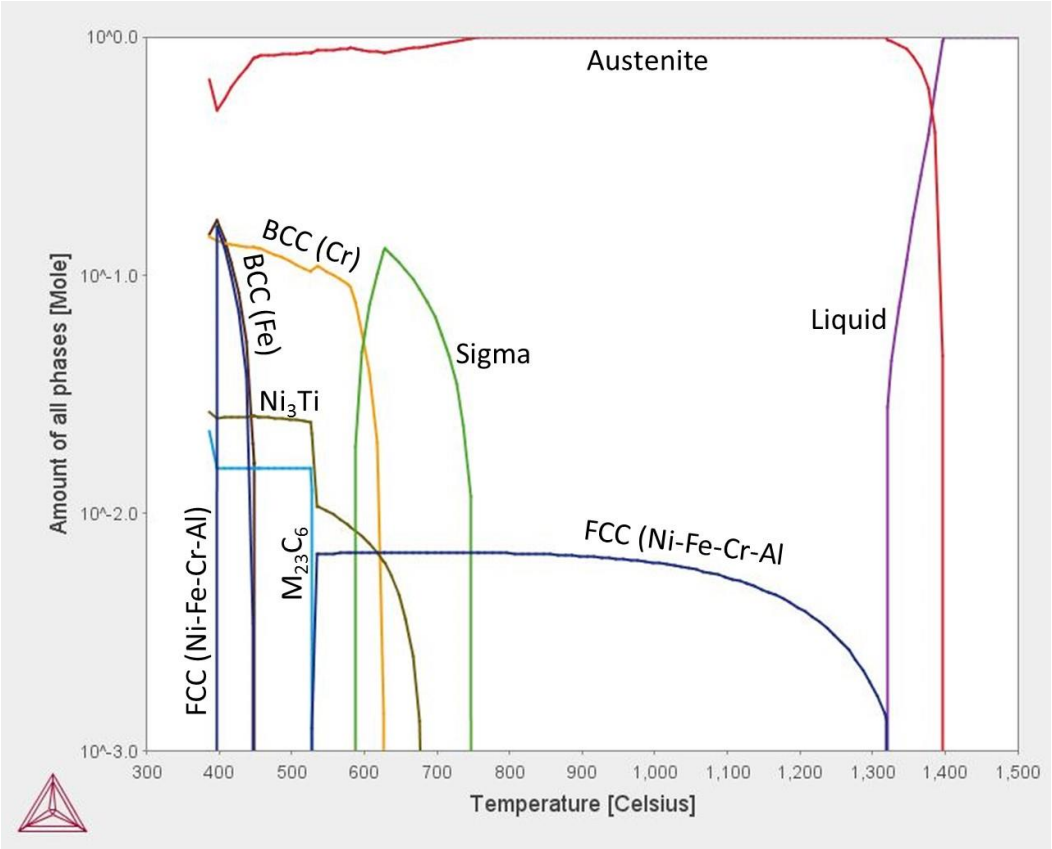

Figure 5-Phase diagram calculated through the command mode in ThermoCalc [NP(*) is ThermoCalc's abbreviation for "the sum of the mole fractions of all phases"]

- Set 1-Only the phases reported by the phase diagram calculated through ThermoCalc
  - Liquid, all FCC phases, all BCC phases, M23C6, SIGMA, and Ni3Ti/GAMMA_PRIME
- Set 2-Suggested phases reported in the works of Dr. Shim
  - Same as previous plus M7C6
- Set 3-Phases known to be present in austenitic stainless steels
  - Same as previous plus CEMENTITE, M6C, LAVES_PHASE, CHI, G-PHASE, and M3C2
- Set 4-All phases recorded within the chosen MatCalc thermodynamic database
  - All allowable phases

MatCalc complex phase diagrams were calculated and evaluated against the ThermoCalc phase diagram for Alloy 800H in order to decide which MatCalc database is best suited to handle Alloy 800H calculations and to determine which set of phases to include in the Alloy 800H precipitation kinetics simulations. Figure 6 depicts the results from using the Fe thermodynamic database (version 2.023). Immediately, it can be seen that the phase transformation between austenite and the liquid phase occurs above 1400˚C. This temperature is unbelievably high and immediately rules out the Fe database for HT calculations. The Fe database does produce a similar looking phase diagram, however the

amount of agreement is still lacking. While looking at these phases the reader should also be aware that there were numerous convergence issues resolving around the BCC_DISL phase, especially with the modified Fe database. Further investigation found that this phase was actually added to aid mobility calculations and was not meant for such calculations. For this reason the phase was removed from the simulation results, however before it was removed, it appeared with a moderately high concentration at temperatures below 450˚C.

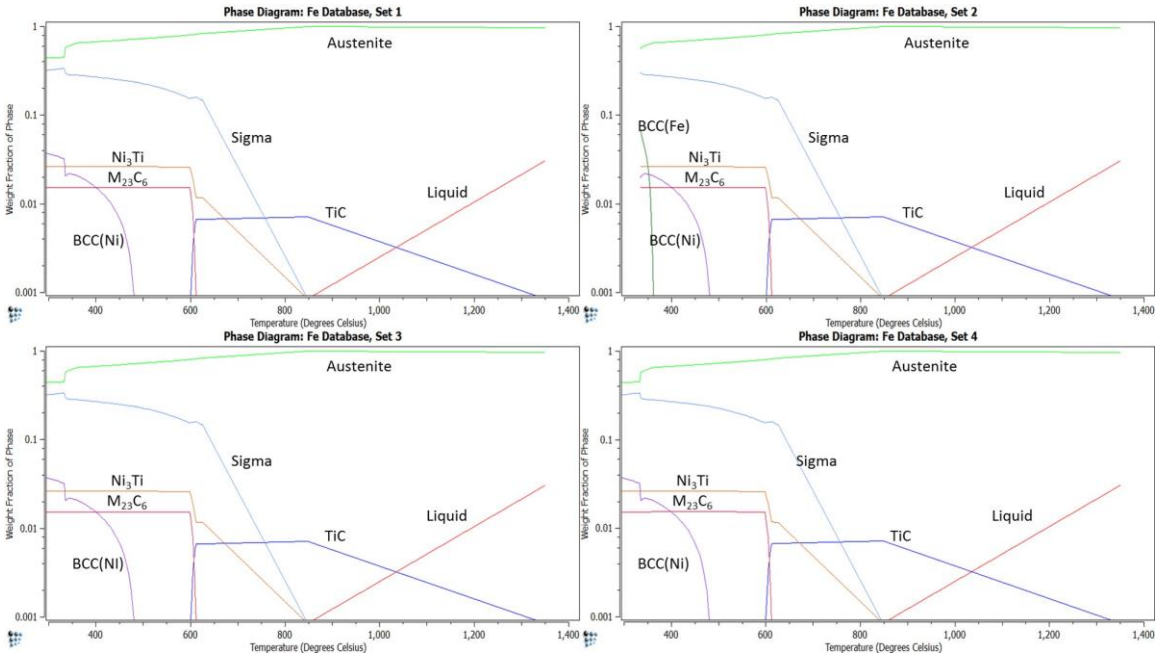

Figure 6-Complex phase diagrams calculated using step equilibrium calculations in MatCalc varying temperature with a step interval of 5. Figure 6 uses the 'mc_fe' (version 2.023) thermodynamic database for stepping calculations.

Figure 7 shows the calculations for the modified Fe database (version 2.003). Note that these figures also predict melting at temperatures in excess of 1400˚C. In addition, spikes of BCC-Fe appear at around 600˚C and with the

majority of the phase forming below 400˚C. These spikes are considered to be convergence issues with the database and the declining peak of Sigma at around 625˚C is thought to be ignored, as well as the corresponding BCC-Fe peak. The only major discrepancy between the Fe database and the modified Fe database is the appearance of BCC-Fe at temperatures below 400˚C. This phase was reported by the ThermoCalc phase diagram, however ThermoCalc reported it for temperatures above 400˚C.

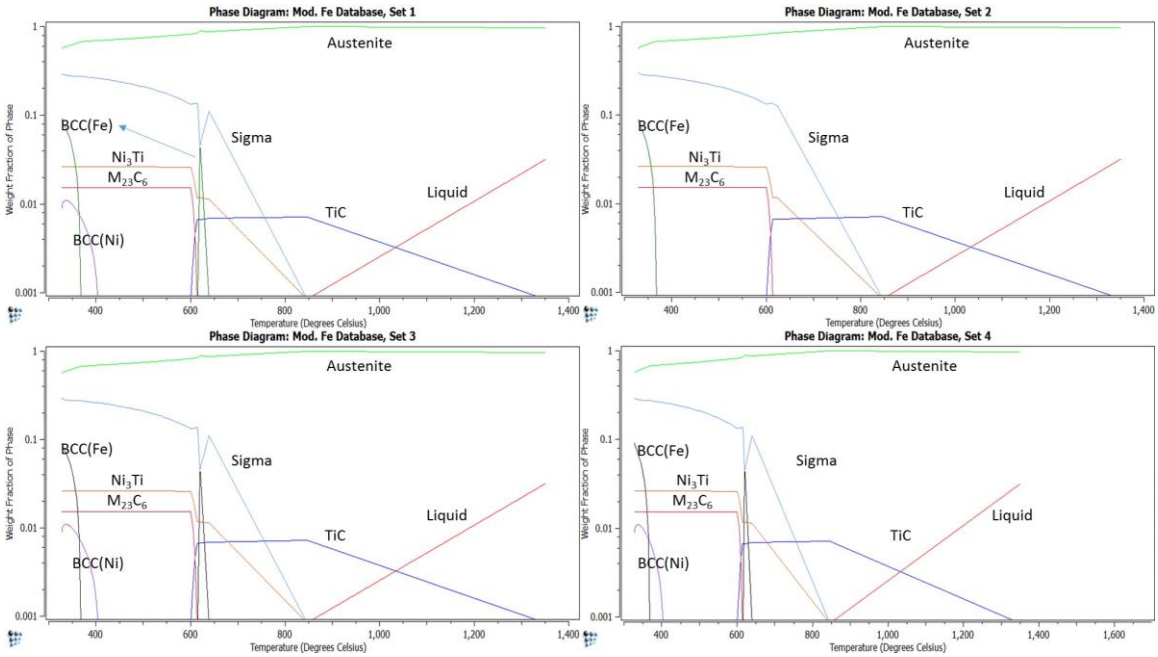

Figure 7-Complex phase diagrams calculated using step equilibrium calculations in MatCalc varying temperature with a step interval of 5. Figure 7 uses the modified 'mc_fe' (version 2.003) thermodynamic database from the results of Shim for stepping calculations [14].

Figure 8 shows the complex phase diagram calculated using the Ni database (version 2.012). Here, melting is found to occur between 1350˚C and

1400˚C, which agrees with the reported melting temperature of the Alloy 800 series at 1357-1385˚C. The agreement between sets 1-4 is also good with the Ni database. The complex phase diagrams calculated from the MatCalc Ni database and ThermoCalc SSOL5 thermodynamic database, found in Figure 5, show good agreement for austenite, BCC-Fe, and liquid phases. In addition, the formation of γ' and $M_{23}C_6$ phases are similar in both programs. Major discrepancies are found between sigma phase and a minor FCC phase in each. Sigma phase was not reported by ThermoCalc at low temperatures. MatCalc reports sigma phase in nearly the exact same amount as ThermoCalc at higher temperatures, however it continues to predict sigma phase at lower temperatures where ThermoCalc reports sigma phase dissolving back into the matrix. This dissolution of sigma phase (which is Cr and Fe rich) then produces the BCC-Cr phase seen in the ThermoCalc phase diagram. Without this phase transformation, the lack of a BCC-Cr phase in the MatCalc calculation can be explained. In addition, an FCC phase is shown in both MatCalc and ThermoCalc phase diagrams between 500˚C and melting. ThermoCalc lists the constituents of this phase as Ni-55 wt%, Fe-34 wt%, Cr-5.8 wt%, and Al-5.5 wt%. MatCalc lists the constituents for the phase in the same region as being titanium and carbon (MatCalc references the phase output as FCC_A1#1). Aside from the discrepancies between the two programs, it can also be noticed that two new phases form in the Set 4 calculation. These two phases, FCC-Cu and HCP-Ni_3Ti, were not reported in the sets with fewer phases considered due to the fact

that they were among the phases not included in those sets. These phases were also not noted in the ThermoCalc results.

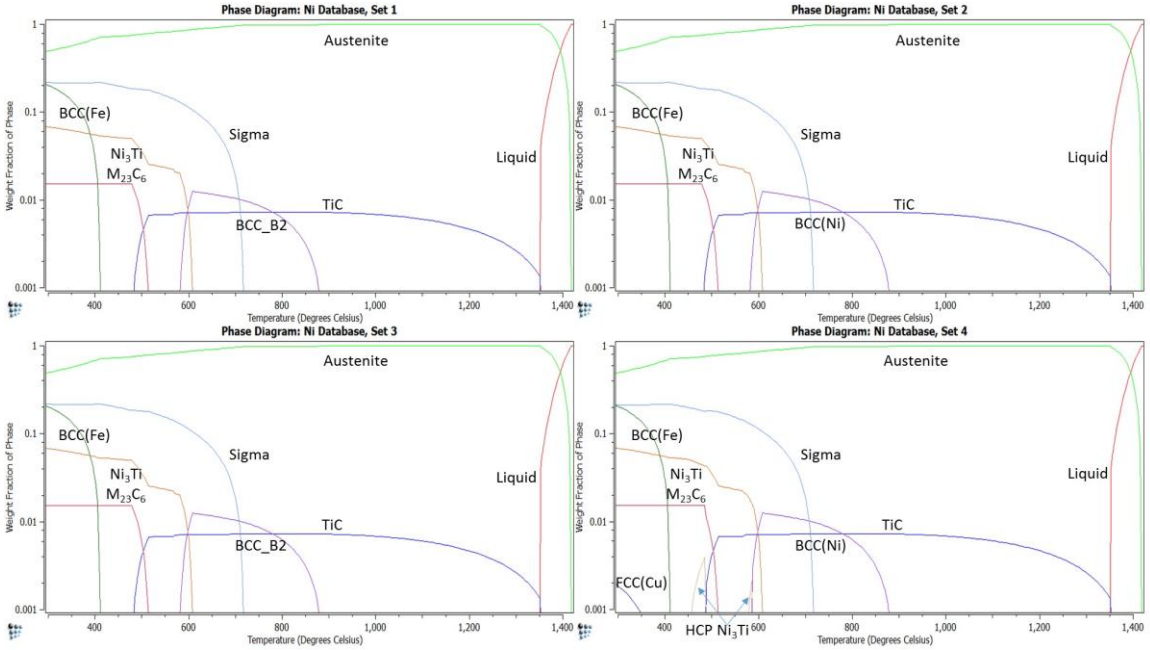

Figure 8-Complex phase diagrams calculated using step equilibrium calculations in MatCalc varying temperature with a step interval of 5. Figure 6 uses the 'mc_ni' (version 2.012) thermodynamic database for stepping calculations.

Figure 9 shows good agreement between sets 1-3 for the modified Ni database (version 2.011), however discrepancies occur between these and set 4. Recall that set 4 is accounting for all phases listed in the database. The major discrepancy in set 4 is the replacement of sigma phase with the HCP-Ni_3Al phase. This phase is similar to the HCP-Ni_3Ti phase predicted to occur in Figure 8 and both are included within the same data set. With either database, this ETA (HCP-Ni_3Ti,Al) phase seems to have convergence issues. Sigma phase is

actually found within the downward spike in the middle of the HCP-Ni_3Al phase in Figure 9. The FCC-Cu phase did not form with the modified Ni database.

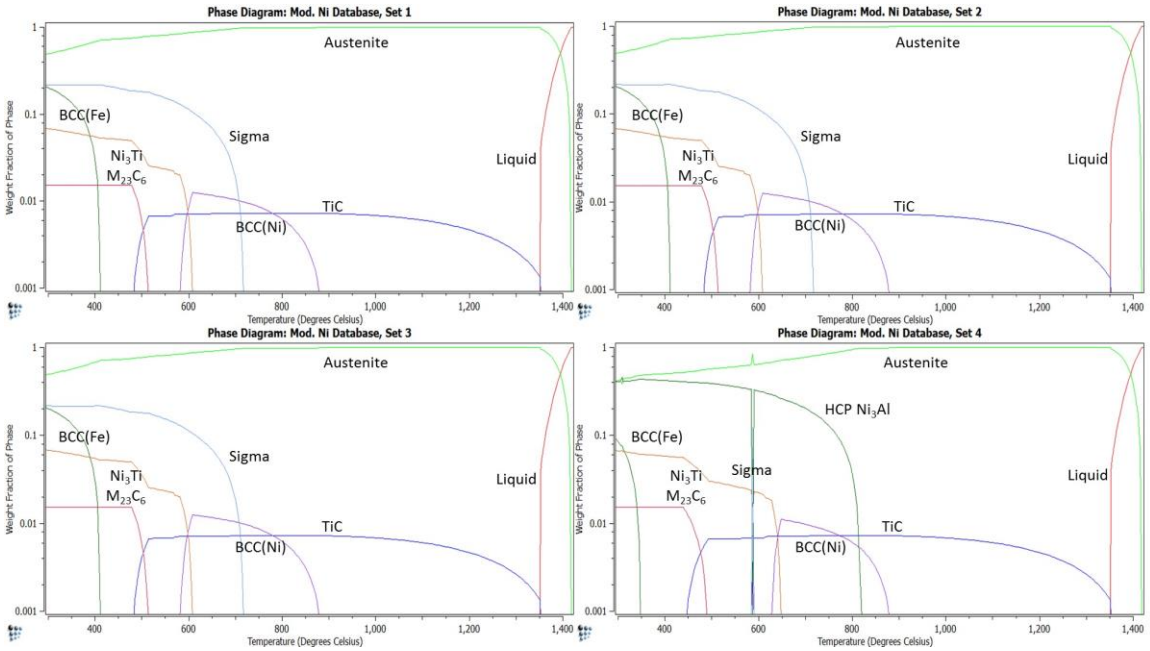

Figure 9-Complex phase diagrams calculated using step equilibrium calculations in MatCalc varying temperature with a step interval of 5. Figure 6 uses the modified 'mc_ni' (version 2.011) thermodynamic database from the results of Shim for stepping calculations.

From the above results, several comparisons can be made between the MatCalc and ThermoCalc databases. The ThermoCalc database shows that sigma phase only nucleates at moderate temperatures (between 600˚C and 750˚C), where the dissolution of sigma at lower temperatures forms BCC-Cr and contributes to a minor increase in the austenitic matrix. MatCalc indicates sigma forming at all temperatures below 700˚C, regardless of the database used. One

possible explanation for this could be the fact that the ThermoCalc SSOL5 database does not focus on high nickel alloys but instead focuses on all solid solutions. It would therefore be expected to have some degree of inaccuracy in regards to calculating complex phase diagrams for a high nickel alloy. Another possibility is that the database from MatCalc has insufficient data regarding the BCC-Cr phase. In either case, the lack of data from either ThermoCalc or MatCalc databases cannot be confirmed due to lack of mention of the sigma phase in current literature at either high or low temperatures. It is therefore my assumption that sigma is a possible precipitate in the larger range until further research can confirm either its presence or absence at low temperatures. The formation of FCC-Cu is also an interesting point to discuss. FCC-Cu (which was only considered in set 4 for each database) was found to precipitate using the Ni databases. This would suggest it as a possible minor phase within the material. Although FCC-Cu does not appear at 400˚C, it will be considered in the MatCalc precipitate kinetics simulations as a possible byproduct of radiation, however it will not be considered as a precipitate due to its coexistence as a minor phase. The ETA phase also appears in the set 4 phase diagrams, however due to the phase existing above the targeted temperature and seeming to have some difficulty with convergence it will not be considered in the precipitation kinetics simulations.

From these results, the best MatCalc database is one of the nickel databases. Due to the complete replacement of sigma by the ETA phase and

lack of any other significant changes, the unmodified Ni thermodynamic database (version 2.012) was selected for future Matcalc calculations. Based off these results it was decided to include the following phases for all precipitate kinetics simulations: Liquid, FCC_A1, BCC_A2, BCC_B2, GAMMA_PRIME, SIGMA, M23C6, and CuS. In addition, the following phases will be considered as possible precipitates: GAMMA_PRIME, SIGMA, and M23C6. After the previous analysis, Figure 10b was chosen to represent the expected phase behavior of Alloy 800H before irradiation, while keeping in mind the discrepancies between Figure 10 and Figure 5.

Analysis of Figure 10 reveals two major discrepancies between the two programs, keeping in mind that ThermoCalc calculations were conducted using the SSOL5 solid solutions database while the selected MatCalc simulation used the Ni database. First, the prediction of sigma phase is predicted between 590 and 750˚C by ThermoCalc, while MatCalc predictions show it to appear anywhere below 720˚C. Second, the FCC phase formed at low phase fraction between 500˚C consists of different major constituents. ThermoCalc reports this phase to consist of Ni, Fe, Cr, and Al constituents while MatCalc designates this as a TiC phase. The presence of sigma is most interesting due to the fact that it is not mentioned in the literature. Despite this, both databases do show formation of sigma phase in Alloy 800H. In order to determine whether sigma phase should be present, the MatCalc 800H complex phase diagram was re-calculated for sets 1-4 using the Ni database. The results, found in Figure 11,

show conclusively that MatCalc cannot resolve the phase equilibrium of Alloy 800H using the Ni database without sigma phase. In addition, ternary phase diagrams were calculated for the Fe-Ni-Cr system using ThermoCalc. These diagrams, shown in Figure 28Figure 34 in the Appendix, show phase equilibrium for Fe-Ni-Cr at 200, 400, 600, 800, 1000, 1200, and 1350˚C. These diagrams support the presence of a sigma phase at 600 and 800˚C, but not at 400 or 1000˚C.

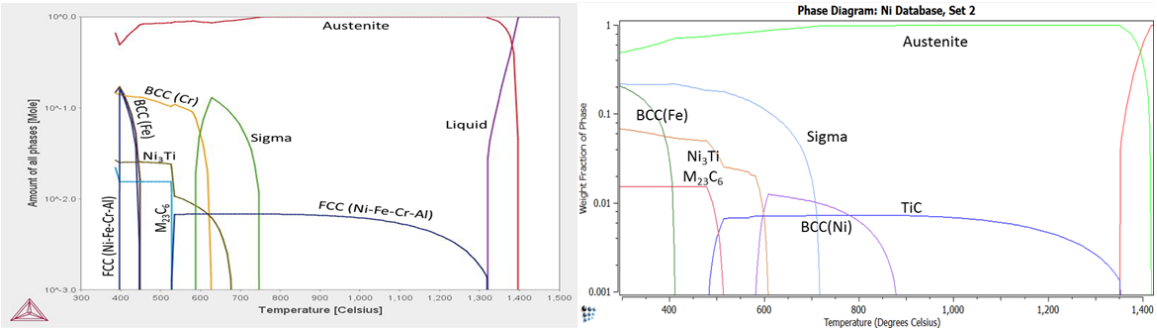

Figure 10-Selected phase diagram from a) the ThermoCalc complex phase diagram calculation and b) the selected aging simulations from Figure 8 to best represent MatCalc projections for Incoloy Alloy 800H.

Calculation of Figure 11 and the Fe-Ni-Cr ternary phase diagrams supports the presence of a sigma phase, however they do not help to determine whether sigma phase should only form at moderate temperatures or at moderate and low temperatures. Further analysis of the ThermoCalc and MatCalc phase diagrams reveals that in the ThermoCalc phase diagram, the sigma phase dissolves into BCC-Cr at low temperatures.

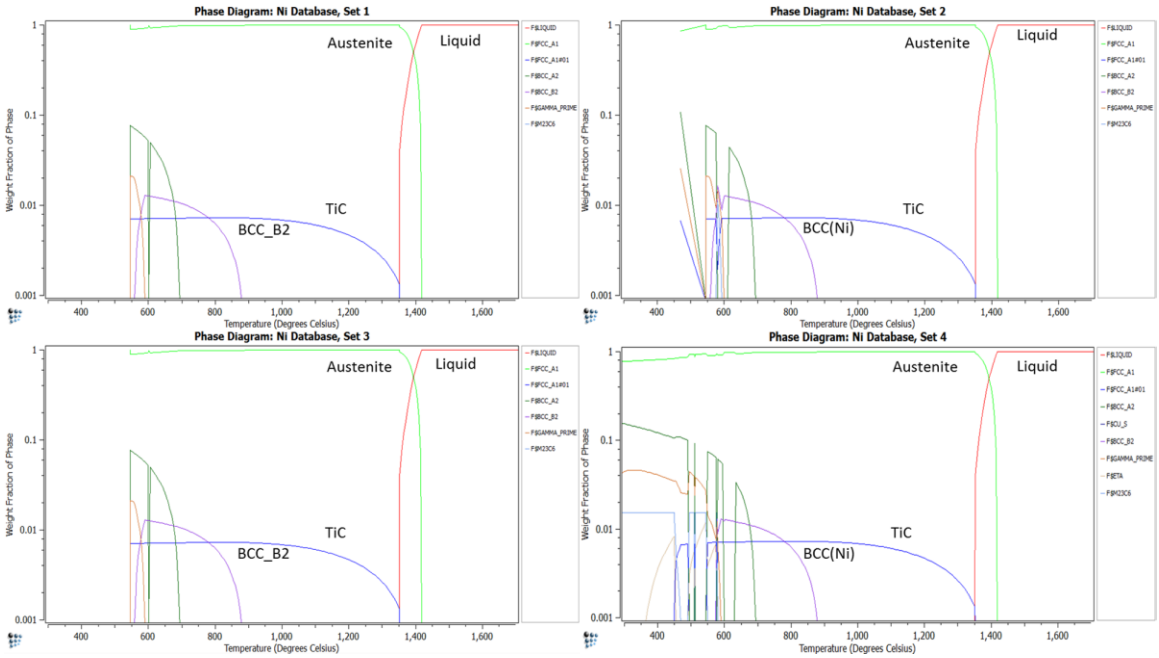

Figure 11-MatCalc complex phase diagrams calculated using the unmodified Ni database for sets 1-4. These diagrams were calculated using the same data that was used in Figure 8, with the only difference being the removal of sigma phase in the program's calculations.

The MatCalc phase diagram does not show a BCC-Cr phase, however does have a BCC-Fe phase. Another graph was calculated in MatCalc, duplicating this BCC-Fe phase and appending its constituency to being Cr-based instead of Fe-based. This graph found more success, and with a few other modifications to the constituency of phases considered by MatCalc Figure 12 was created. These modifications accounted only for the differences between ThermoCalc and MatCalc diagrams which had only been calculated. One such change was in altering the constituency of the FCC-TiC phase to being FCC-Fe, Ni, Cr, Al. It can be seen that this phase diagram is very similar to the original ThermoCalc phase diagram calculated for Alloy 800H.

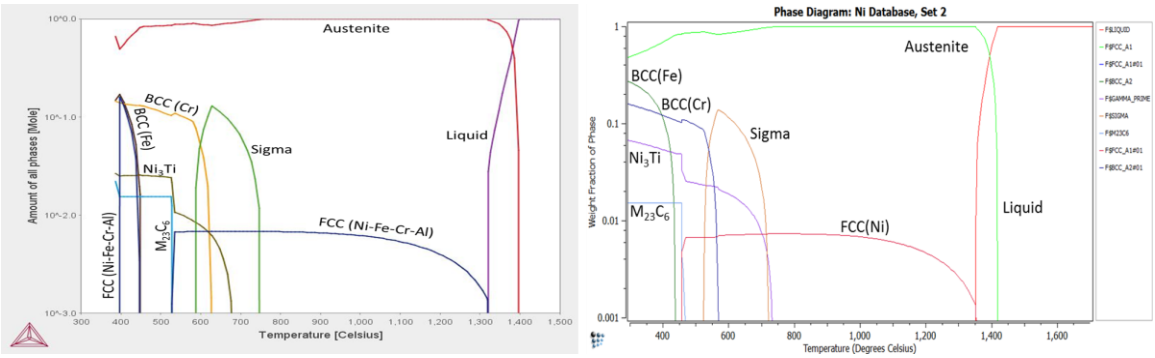

Figure 12-Comparison of a) ThermoCalc complex phase diagram for unirradiated 800H and b) Selected MatCalc phase diagram from Figure 8 after adjustments to phase compositions including the addition of BCC-Cr and the altercation of FCC-TiC to FCC-Ni.

Additionally, complex phase diagrams were calculated in both ThermoCalc and MatCalc for the assumed alloy chemistry resulting from RIS at a radiation exposure of 5, 10, and 20 dpa found in Table 3. It can be seen that in Figure 13 there is much less agreement between ThermoCalc and MatCalc than the 0 dpa phase diagrams. The same type of adjustments were made in calculating the 5 dpa MatCalc phase diagrams as were used to produce the 0 dpa MatCalc diagram. Major differences include $M_{23}C_6$ forming at a larger temperature range in MatCalc simulations, Ni_3Ti forming in significantly larger amounts in MatCalc, lessening of BCC-Cr in MatCalc, and the amount of the matrix phase austenite at low temperatures. In addition, before adjustments were made, MatCalc was predicting sigma phase from 400 to 800˚C in significant (~0.1 wt fraction) amounts in the place of BCC-Cr. Prior to these adjustments MatCalc also predicted no FCC-TiC or FCC-Cu phases. Part of the adjustments made for this was to remove the sigma phase completely from the phase

considerations. It should also be noted that MatCalc did not show much change in the melting point temperature range, either before or after adjustments to phase compositions, while the melting point temperature does drop notably in the ThermoCalc phase diagram.

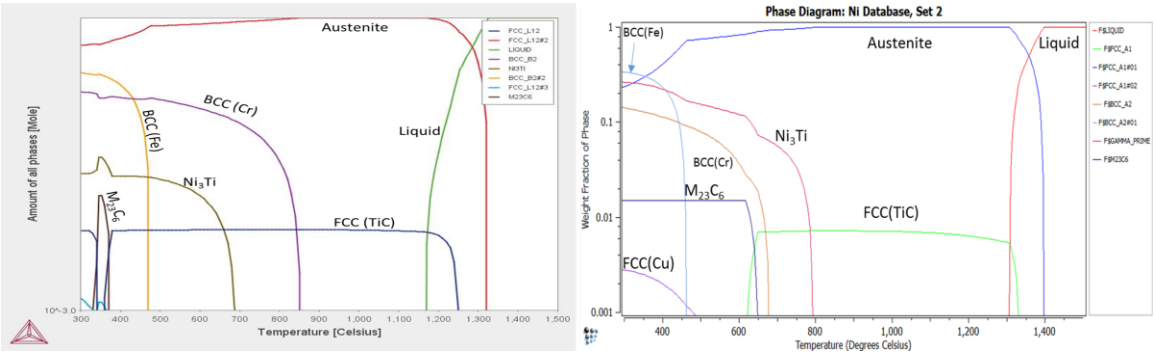

Figure 13-Comparison between the a) ThermoCalc complex phase diagram calculated using the compositional adjustments to Alloy 800H representative of 5 dpa neutron damage. b) the complementary MatCalc complex phase diagram corrected in attempt to match the ThermoCalc equivalent.

At the composition reflecting the assumed RIS at 10 dpa from Table 3 we see significant widening and reduction of the melting point in the ThermoCalc phase diagram. Similar observations can be made with the MatCalc phase diagram. Unlike the 0 and 5 dpa MatCalc phase diagrams, the 10 dpa diagram could not be well adjusted to match the ThermoCalc phase diagram. This was due to the formation of the Ti_3SiC_2 phase by ThermoCalc. This phase is not recorded in the MatCalc Ni database and could therefore not be accounted for by the program in calculating the phase diagram. For this reason, the MatCalc

phase diagram shown in Figure 14 is the phase diagram calculated with the raw phase data without appending any of the phases in the phase status command log. At 10 dpa it can be observed that the formation of sigma is predicted only in the MatCalc phase diagram. The combined formation of BCC-Cr and sigma in MatCalc is similar to the formation of BCC-Cr in ThermoCalc. Formation of Ni_3Ti is much larger in both amount and temperature range in the MatCalc predictions. ThermoCalc also produces Ti_3SiC_2 and FCC-TiC while MatCalc only produces $M_{23}C_6$.

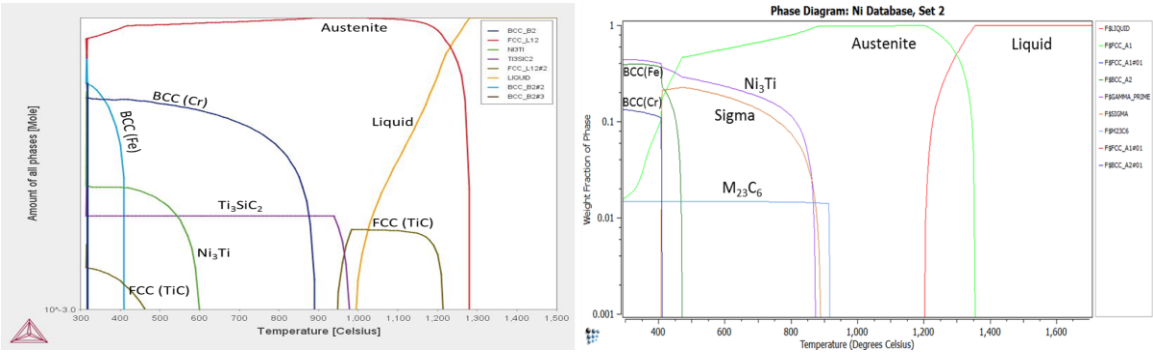

Figure 14-Calculated complex phase diagrams to reflect 10 dpa neutron damage from ThermoCalc and MatCalc.

There is no notable change between the 10 dpa phase diagrams and the 20 dpa phase diagrams. Similar to the 10 dpa diagrams, the 10 dpa diagrams could also not be adjusted due to the formation of the Ti_3SiC_2 phase.

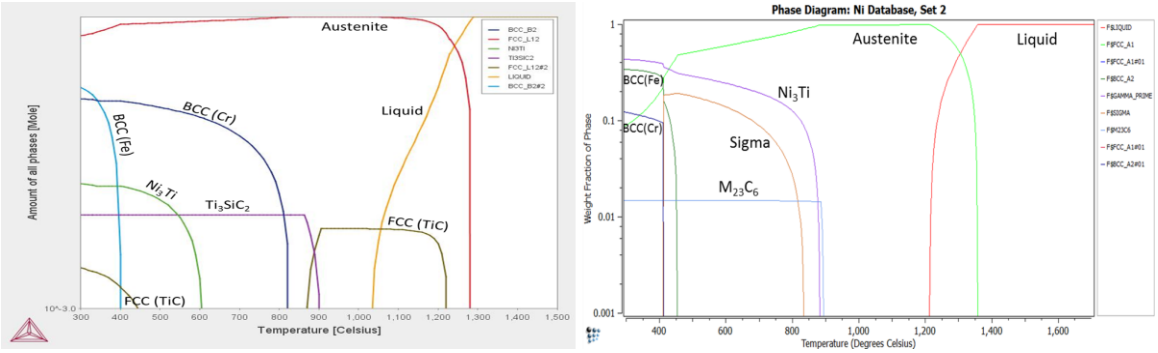

Figure 15- Calculated complex phase diagrams to reflect 20 dpa neutron damage from ThermoCalc and MatCalc.

4.2 Isopleths and RIS behavior

Isopleths mapped using the composition found in Table 3 can be found in Figures Figure 16-Figure 19. Four composition markers have been placed on each graph to mark, Gan's composition (red), the upper and lower bounds for the solution annealed material (black), and the expected composition at 20 dpa (blue). It should be noted that Si is not in the Alloy 800H specification and thus does not have the two black markers. The composition revealed in Figure 16 reveals austenite, several BCC phases, a secondary FCC phase, $M_{23}C_6$, and sigma as possible constituents before radiation. Chromium segregation due to radiation does not result in the crossing of any major phase boundaries at 400˚C and thus should not cause any significant changes in the types of phases that could nucleate (no RIP's expected), however it will likely still affect the predicted amount of some phases, for instance the amount of $M_{23}C_6$ will likely decrease

due to a decrease in chromium. The amount of sigma would also be expected to decrease since it is chromium dependent.

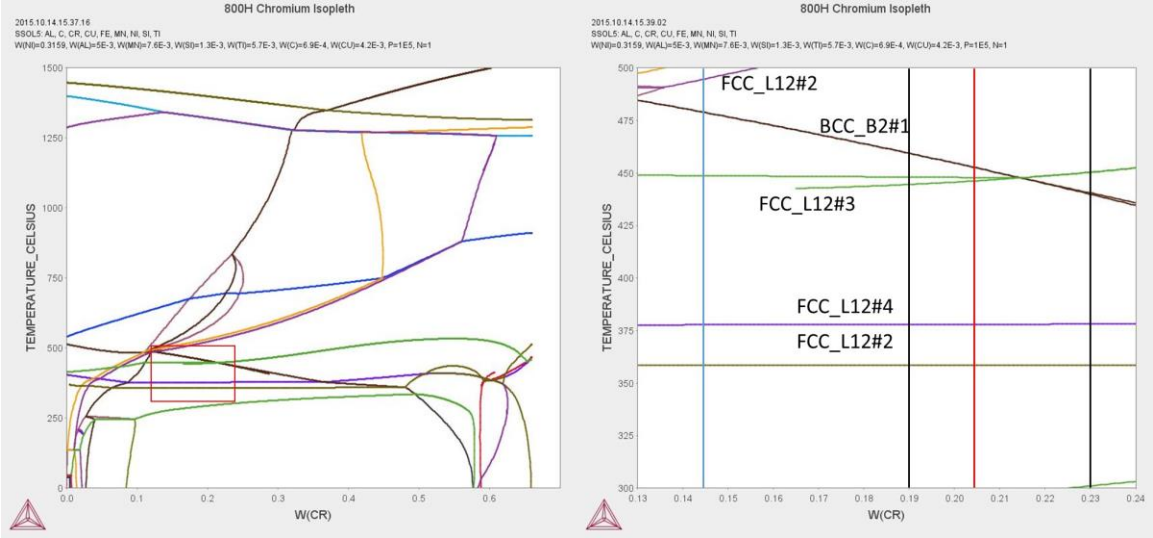

Figure 16-Chromium isopleth calculations carried out with ThermoCalc by varying the chromium content in Alloy 800H from 0 to 1 wt%. The image on the left shows the area the simulation was able to resolve. The image on the right shows area of interest. The two vertical black lines on the right image represent the compositional limits of Alloy 800H. The vertical red line represents the composition of Alloy 800H used for simulations. The vertical blue line represents the expected extent of RIS.

Figure 17 reports the same phases as Figure 16 in the region of interest, except sigma is interchanged with Ni_3Ti. The unirradiated area of interest shows little variance at the target temperature. Radiation is expected to increase the Ni concentration at grain boundaries to around 43%. Similar to the Cr distribution, this increase in Ni is not expected to affect the types of phases which nucleate, although it might have some effect on how much of each phase is present. In particular, it should be expected that the gamma prime phase (Ni_3Ti) will be

produced more at grain boundaries, however it is possible that intergranular Ni_3Ti will decrease slightly.

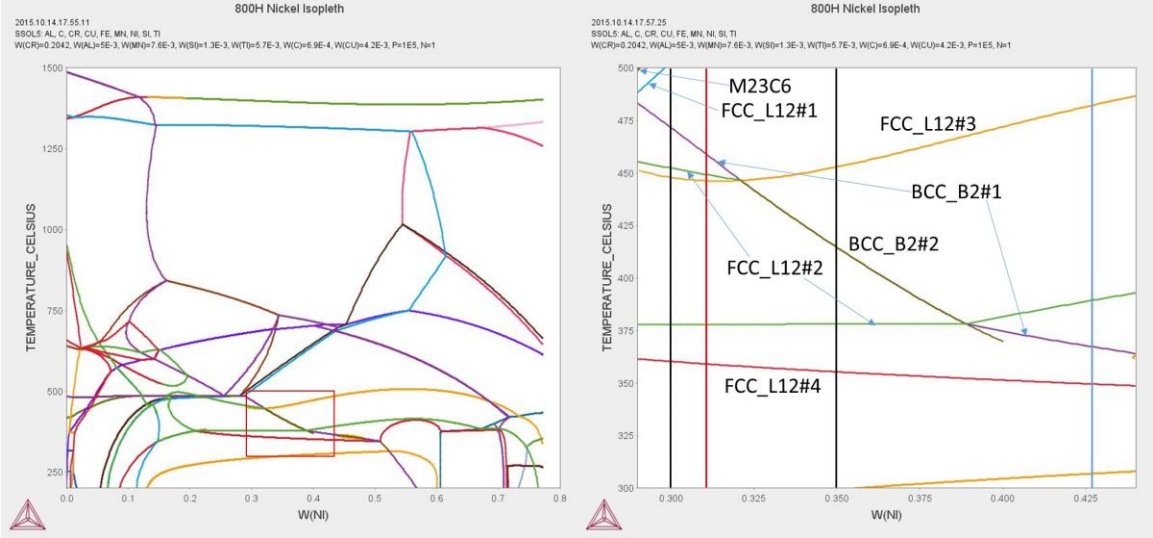

Figure 17-Nickel isopleth calculations carried out with ThermoCalc by varying the nickel content in Alloy 800H from 0 to 1 wt%. The image on the left shows the area the simulation was able to resolve. The image on the right shows area of interest. The two vertical black lines on the right image represent the compositional limits of Alloy 800H. The vertical red line represents the composition of Alloy 800H used for simulations. The vertical blue line represents the expected extent of RIS.

Figure 18 shows the same phases as the previous isopleths in the unirradiated composition range. As with the previous two isopleths, no change is expected due to RIS at grain boundaries, however it is noticeable that the Ni_3Ti phase boundary exists at lower concentration. Although titanium is expected to migrate from the grains to grain boundaries and other sinks, it is not expected that the concentration within the grains should decrease sufficiently enough to cross that phase boundary. Still, it could be noted that any decrease

intergranularly could result in a dramatic decrease in Ni_3Ti since this phase is more commonly found to precipitate intergranularly.

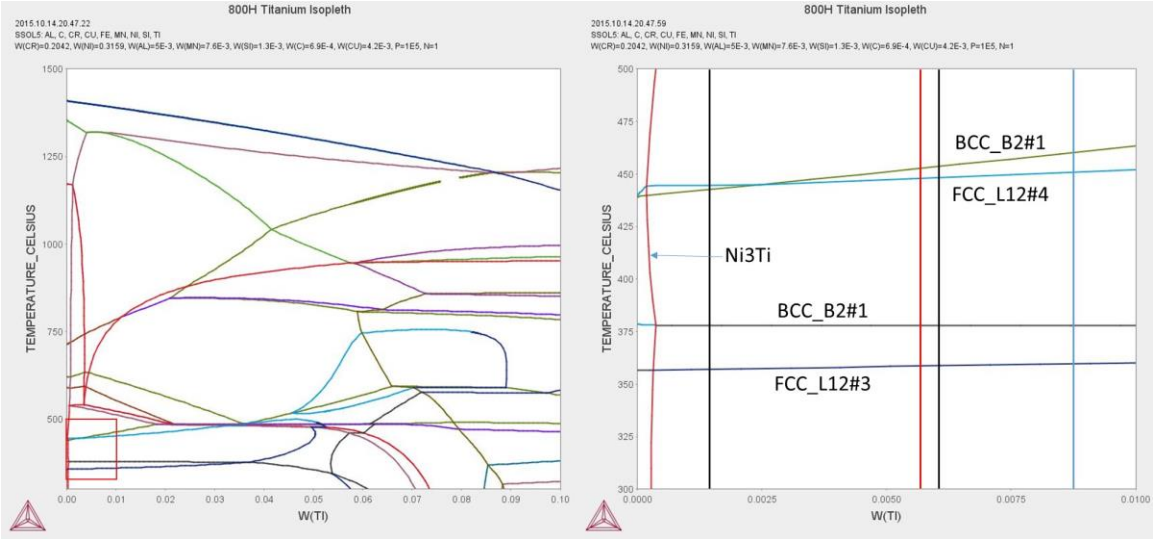

Figure 18-Titanium isopleth calculations carried out with ThermoCalc by varying the titanium content in Alloy 800H from 0 to 0.1 wt%. The image on the left shows the area the simulation was able to resolve. The image on the right shows area of interest. The two vertical black lines on the right image represent the compositional limits of Alloy 800H. The vertical red line represents the composition of Alloy 800H used for simulations. The vertical blue line represents the expected extent of RIS.

Figure 19 reports the same phases at the unirradiated composition. As the composition of Si increases, it can be noted that three distinct phase boundaries are crossed. The first phase boundary is for the $M_{23}C_6$ phase. This possible dissolution of $M_{23}C_6$ was unexpected and shows that RIS could cause this phase to decrease or even disappear within the grain boundaries. This in addition to the Cr segregation from Figure 16 would suggest that $M_{23}C_6$ precipitation will decrease as the dose is increased. The next two phase boundaries of interest are Ti_3SiC_2 and Cr_3Si. Ti_3SiC_2 is a phase that was seen

previously to appear in the ThermoCalc complex phase diagrams for composition variations assumed due to RIS at dose levels of 10 and 20 dpa neutron damage. The appearance of this phase is supported by ThermoCalc at high doses by calculating phase equilibria and isopleth sections for Si. As this is not mentioned in the literature and it is influenced mostly by the impurity element Si, this will not be considered in the simulations of precipitate kinetics as a possible precipitate. It will, however be suggested for further research. Cr_3Si also appears at higher doses. This phase has not yet been noted by any models in this study or in the literature and thus will be considered a minor plausible phase only. It will not be considered in precipitate kinetics calculations, although it could be suggested that large enough precipitation of this may reduce the amount of $M_{23}C_6$ produced at high doses.

4.3 Simulations of Precipitate Kinetics

The simulations of precipitation kinetics during assumed operations were calculated to predict both number density (in $\#/m^3$) and diameter of precipitate particles (in meters). The phases included in the calculation were LIQUID, FCC_A1, BCC_A2, BCC_B2, GAMMA_PRIME, SIGMA, M23C6, ETA, and CuS with GAMMA_PRIME, SIGMA, and M23C6 set as possible precipitates. Plotting of the phase diagrams consisted of two parts, a solution anneal and the representative aging during simulating operating conditions. For the solution anneal the material was heated for 30 minutes (1800 seconds) to 1177˚C, annealed for 2.25 hours (8100 seconds), and then water quenched (5 seconds).

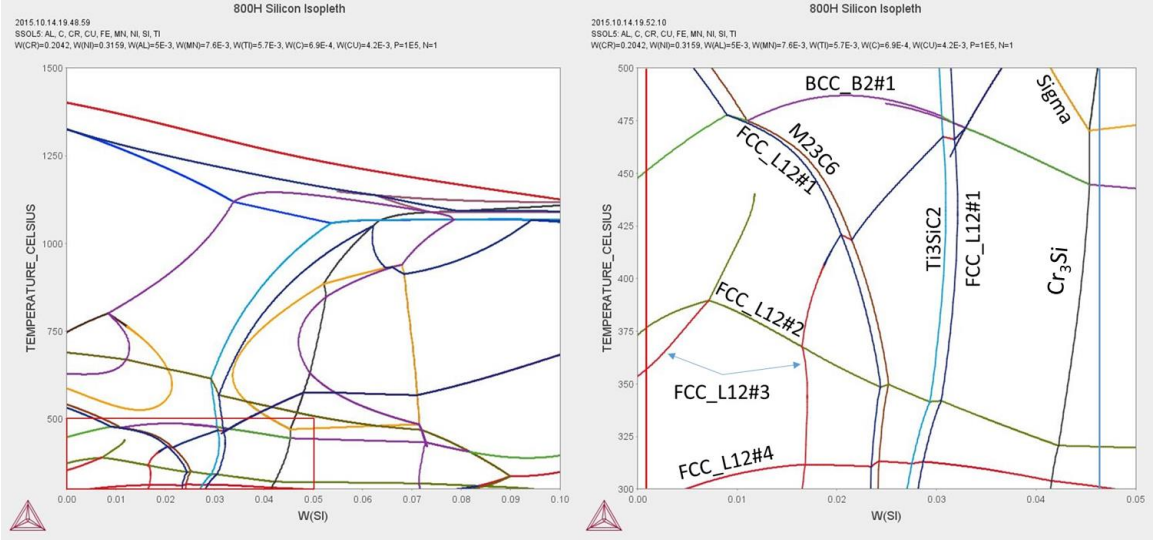

Figure 19-Silicon isopleth calculations carried out with ThermoCalc by varying the silicon content in Alloy 800H from 0 to 0.1 wt%. The image on the left shows the area the simulation was able to resolve. The image on the right shows area of interest. The two vertical black lines on the right image represent the compositional limits of Alloy 800H. The vertical red line represents the composition of Alloy 800H used for simulations. The vertical blue line represents the expected extent of RIS.

The next part of the overall aging procedure consists of a ramp up to 400˚C in 30 minutes, after which the temperature was sustained for 100 years. In Figures Figure 20-Figure 23, the first vertical black line indicates the point at which the solution anneal reached its maximum temperature. The second black line represents the quenching at the end of the solution anneal. The third black line represents the point at which the second segment of the aging simulation reaches maximum temperature (400˚C).

Figure 20 shows the predicted precipitate kinetics results from the aging simulation prior to in-reactor service. During solution annealing the only notable precipitate is $M_{23}C_6$. The maximum number density and precipitate size for

$M_{23}C_6$ during solution annealing are $9.8x10^{21}m^{-3}$ and 35.7nm respectfully. It can be noted that $M_{23}C_6$ nucleates at a larger number density than the other two precipitates throughout the treatment until the very end when it begins to decrease in number. This phenomenon is consistent with Ostwald Ripening. It is likely that the larger $M_{23}C_6$ precipitates are beginning to consume the smaller $M_{23}C_6$ precipitates. Nucleation for sigma and ɣ' continues longer than that for $M_{23}C_6$, although at a much slower nucleation rate. The maximum number densities for $M_{23}C_6$, sigma, and ɣ' are $1.2x10^{22}m^{-3}$, $4.6x10^{21}m^{-3}$, and $1.0x10^{21}m^{-3}$ respectfully. Peak precipitate sizes for each are 23nm, 41 nm, and 39nm respectfully with $M_{23}C_6$ still growing at the end of 100 years of operation. It should also be noted that the peak precipitate size for $M_{23}C_6$ prior to recombination is around 14nm.

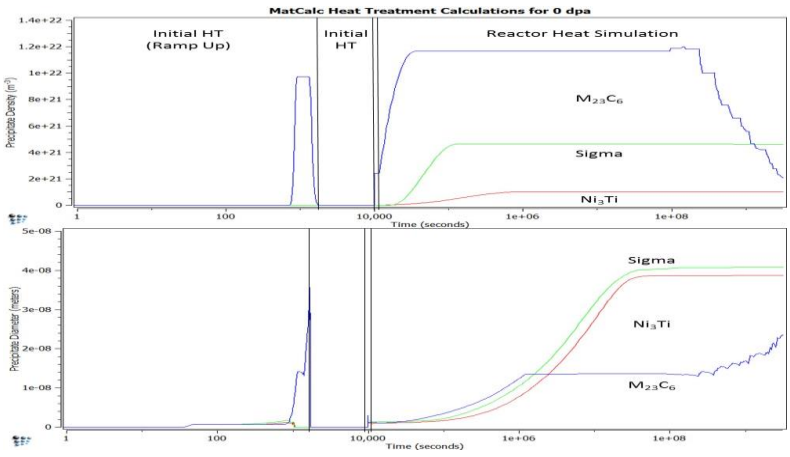

Figure 20-Precipitate kinetics calculated using the 0 dpa compositional estimations from Table 3. The vertical black lines depict different segments of the simulated heat treatment. The first black line indicates the point where the solution anneal reaches its maximum temperature (1177˚C). The second black line represents the quench following the initial solution anneal. The third line represents the point at which the reactor temperature stabilizes (400˚C).

Figure 21 shows the expected precipitate density and size for the assumed composition from Table 3 based on RIS following neutron irradiation to 5 dpa. It can clearly be seen that $M_{23}C_6$ still dominates the solution annealing process. It can be seen that between 0 and 5 dpa very little change is expected with the size of $M_{23}C_6$ precipitates, although the number density does drop considerably. Noticeable changes in Ni_3Ti do occur, however as both the precipitate size and density increases. Due to the fact that this phase tends to precipitate at intergranular dislocations, this might not be cause for concern but it does warrant possible concerns towards grain boundary integrity. It can also be noticed that sigma phase is predicted to produce a higher number density of smaller precipitates. The amount of $M_{23}C_6$ produced after the precipitate growth event decreases from 0 to 5 dpa, however the final average size of precipitates does not change.

For the assumed composition from Table 3, corresponding to RIS at 10 dpa we see the same trends following the 5 dpa calculation. The size and amount of $M_{23}C_6$ does not change much at all, both the size and density of Ni_3Ti continue to increase quite dramatically, and the amount of sigma continues to increase while the size of sigma precipitates drops. At this composition, the number of sigma precipitates is seen to surpass the number of $M_{23}C_6$ precipitates, while the sizes of all three precipitates reach an apparent steady state.

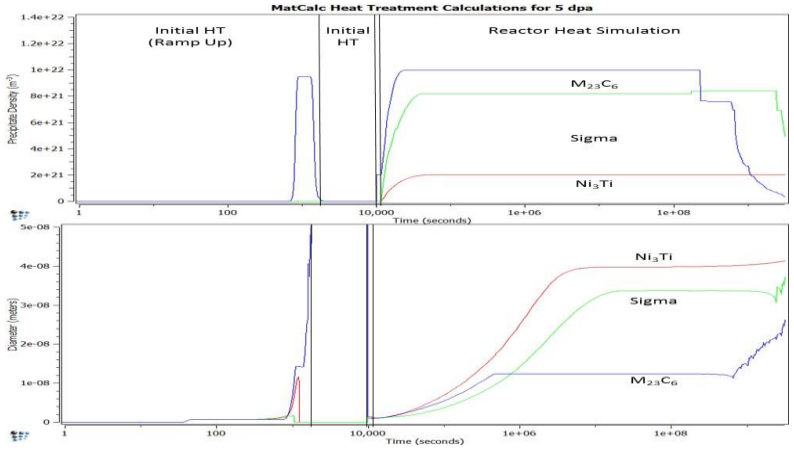

Figure 21-Precipitate kinetics simulation calculated using the 5 dpa compositional estimations from Table 3. The vertical black lines depict different segments of the simulated heat treatment. The first black line indicates the point where the solution anneal reaches its maximum temperature (1177˚C). The second black line represents the quench following the initial solution anneal. The third line represents the point at which the reactor temperature stabilizes (400˚C).

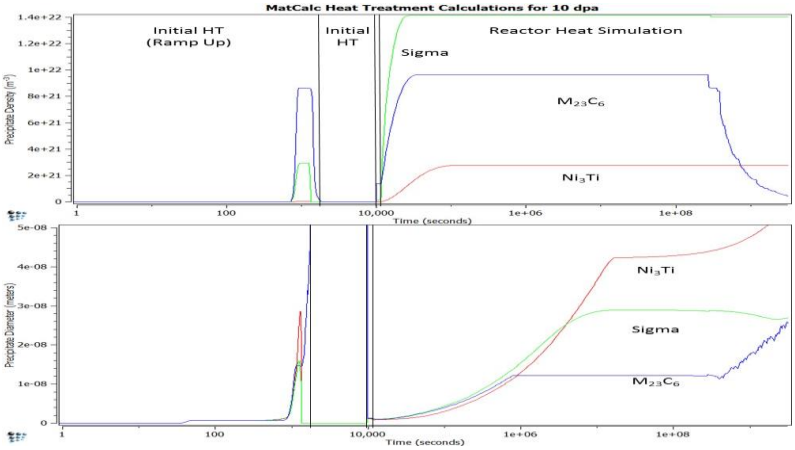

Figure 22-Precipitate kinetics simulation calculated using the 10 dpa compositional estimations from Error! Reference source not found.**. The vertical black lines depict different segments of the simulated heat treatment. The first black line indicates the point where the solution anneal reaches its maximum temperature (1177˚C). The second black line represents the quench following the initial solution anneal. The third line represents the point at which the reactor temperature stabilizes (400˚C).**

By comparison of Figure 22 and Figure 23, it can be seen that for RIS compositions between 10 and 20 dpa, the amount of sigma reaches a maximum saturation point and begins to decrease. This decrease in the amount of precipitates is not met with any significant change in precipitate size, which would suggest that sigma is beginning to dissolve back into the matrix. Little else changes during the assumed RIS composition changes during reactor operation between 10 and 20 dpa.

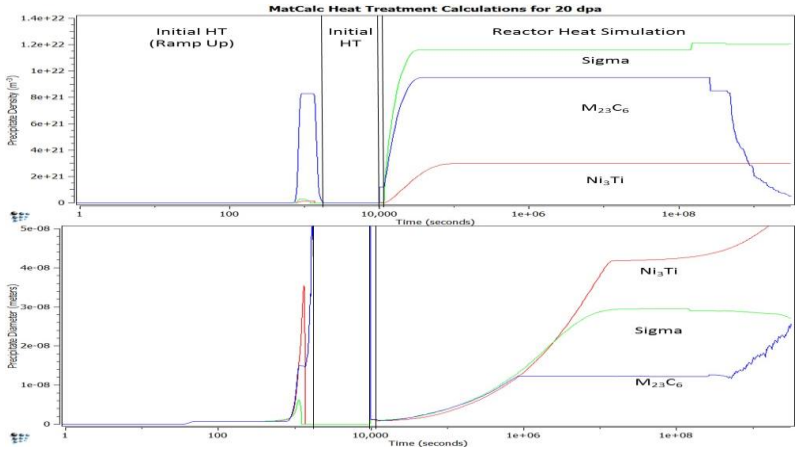

Figure 23-Precipitate kinetics simulation calculated using the 20 dpa compositional estimations from Error! Reference source not found.**. The vertical black lines depict different segments of the simulated heat treatment. The first black line indicates the point where the solution anneal reaches its maximum temperature (1177˚C). The second black line represents the quench following the initial solution anneal. The third line represents the point at which the reactor temperature stabilizes (400˚C).**

To summarize the calculations of precipitation kinetics, it has been noticed that for $M_{23}C_6$ the precipitate size is expected to remain small in comparison to the other precipitates. No real size change is seen in $M_{23}C_6$ as dose increases, however the number density of precipitates does decrease. This agrees with the expectations of the effects of RIS on chromium segregation in alloy 800H.

Ostwald Ripening is also shown to occur in $M_{23}C_6$, beginning between 6 and 7 years into reactor operation. This phenomenon results in the dissolution of smaller $M_{23}C_6$ precipitates into larger $M_{23}C_6$ precipitates resulting in a stepwise drop in precipitate density and an increase in precipitate size. The overall decrease in the amount of $M_{23}C_6$ precipitates at grain boundaries would be expected to reduce stresses at grain boundaries and help improve grain boundary cohesion. Ostwald Ripening could lead to problems during lengthy reactor operations as precipitates migrate and begin to grow. The growth of these precipitates is not widely dramatic, as the timescale is long, however the amount of growth could be cause for concern as it could jeopardize grain boundary cohesion. It should also be mentioned that Cr segregation occurs as chromium migrates away from grain boundaries and sinks. $M_{23}C_6$ is known to nucleate at both grain boundaries and dislocation sites. Due to this it could be expected to see a slight increase in the amount of $M_{23}C_6$ produced intragranularly.

Sigma phase precipitates are among the largest predicted precipitates when no radiation effects are applied, however increasing dose seems to lower the final precipitate size after 100 years from 41nm to 29nm (a 28% size reduction). In contrast, the size of sigma precipitates is seen to increase with increasing dose until it saturates somewhere between 10 and 20 dpa. Prior to this sigma appears to begin to re-dissolve back into the matrix. This represents typical precipitate growth as sigma precipitates begin to nucleate and grow, the

precipitates begin to congregate as they migrate through the lattice and merge to minimize free energy resulting in larger precipitates, until the matrix begins to re-dissolve the precipitates. Due to the fact that sigma phase is only expected to precipitate in grain boundaries, this could affect the cohesiveness of grain boundaries. The presence of sigma at grain boundaries might also lead to reduced corrosion resistance, which could result in stress corrosion cracking.

Ni_3Ti precipitation, however is not predicted to be much cause for alarm. With increasing dose Ni_3Ti precipitates are seen to increase in both size and number. This increase is much less dramatic than the changes seen in the other two precipitates, however, and appears to mostly saturate somewhere between 10 and 20 dpa. Ni_3Ti, however is not expected to precipitate particularly at grain boundaries, but instead precipitates at dislocation sites. It is possible for these precipitates to form near grain boundaries, however, so these results will be used only from that perspective. It could also be inferred that with reversed effects from RIS, the nucleation of Ni_3Ti precipitates will have opposite results. Due to RIS not having significant effects within grains apart from heightened mobility, it would be expected that Ni_3Ti precipitate evolution would result in either precipitates of the same size and density as those predicted in the 0 dpa simulation (Figure 20) or in smaller, less dense precipitates as those found in Figure 20.

CHAPTER V

CONCLUSIONS AND RECOMMENDATIONS

5.1 Conclusions

Comparison of ThermoCalc and MatCalc phase diagrams was conducted to find many commonalities as well as a few discrepancies. Differences in the range of temperature required for sigma phase to be present were among the most concerning. The presence of sigma phase in Alloy 800H could not be confirmed by the literature for purposes of this project, however sigma phase is a common precipitate in many austenitic stainless steels. In addition, it was not possible to calculate phase diagrams without the presence of sigma phase in MatCalc and sigma phase was observed in the Fe-Ni-Cr ternary, supporting the presence of sigma phase in Alloy 800H. After analyzing the complex phase diagrams it was decided that the most likely precipitates were $M_{23}C_6$, Sigma, and Ni_3Ti.

Isopleths for Cr, Ni, Ti, and Si were calculated and analyzed to better understand the effects of RIS. The two major isopleths (Cr and Ni) revealed little concern in the way of producing RIP's, although it was noted that they would have an effect on the amount of each precipitate would be produced. Notably that Cr depletion at grain boundaries will result in a reduced amount of $M_{23}C_6$ and Ni enrichment at grain boundaries could result in an increased amount of Ni_3Ti

produced around grain boundaries at dislocation sites. Ti enrichment would also encourage Ni_3Ti nucleation near grain boundaries. Observation of the Si isopleth showed the possible production of an unknown Si-based phase. This phase was noted for future research, however was not included in phase predictions due to being a minor phase.

Precipitate kinetics simulations found Ostwald Ripening to occur in $M_{23}C_6$, beginning at 6+ years of operation. This results in a steady increase in average $M_{23}C_6$ size, which nearly doubled over the remaining reactor operations time (93-94 years). The growing amount of sigma phase was also cause for concern. It was seen that as the dose increased, the amount of sigma phase expected to be produced increased until saturation between 10 and 20 dpa. The reduction of sigma precipitate density following saturation was not met with any reduction in size. Thus at higher doses it is likely that sigma phase will be less important to phase stability.

5.2 Recommendations

To determine the full extent of the results from this work it is important to understand more about the role of sigma phase in Alloy 800H. Published literature results do not mention the presence of any sigma phase in Alloy 800H despite the prediction from both MatCalc and ThermoCalc thermodynamic models that sigma phase is a constituent, at least at high temperatures, of this material.

Several other minor phases were also discovered through these analyses. ETA (hexagonal Ni_3Ti,Al), FCC-Cu, and Ti_3SiC_2 were noted as minor phases through either the calculation of complex phase diagrams or isopleths. The effects of these phases on Alloy 800H should also be analyzed to determine if any of these present a threat to the material's lifetime or stability.

Thermomechanical processing was also a large topic in the literature. Although some research was conducted experimentally to determine how this would impact radiation resistance, the results of which concluded that TMT had a positive impact on radiation resistance, it would be beneficial to conduct modeling similar to the current work which included TMT pre-treatments. Unfortunately, integrating the cold working process was outside the scope of the current works and the TMT process could not be included in the precipitate kinetics simulations.

LIST OF REFERENCES

1. Ren, W., *Status of Alloy 800H in Considerations for the Gen IV Nuclear Energy Systems*. 2014.
2. Cao, Y., *The Impact of Aging Pre-treatment on the Hot Deformation Behavior of Alloy 800H at 750C.* Journal of Nuclear Materials, 2014. **452**: p. 77-86.
3. Gan, J., *Irradiated Microstructure of Alloy 800H.* Journal of Nuclear Materials, 2006. **351**: p. 223-227.
4. SpecialMetals, *INCOLOY Alloy 800H & 800HT*. 2004.
5. Sabharwall, P., *Feasibility Study of Secondary Heat Exchanger Concepts for the Advanced High Temperature Reactor*. 2011.
6. Allen, T., *Grain Boundary Engineering and Radiation Resistance of GFR Candidate Metallic Materials*. 2006.
7. Gutierrez, A., *Laser-Surface-Alloying of the Iron Based Superalloy Incoloy-800H with Al.* Applied Physics A, 1996. **63**: p. 461-465.
8. Tan, L., *Thermomechanical Treatment for Improved Neutron Irradiation Resistance of Austenitic Alloy (Fe-21Cr-32Ni).* Journal of Nuclear Materials, 2013. **437**: p. 70-74.
9. Tan, L., *An Electron Backscattered Diffraction Study of Grain Boundary-Engineered INCOLOY Alloy 800H.* Metallurgical and Materials Transactions A, 2005. **36A**.
10. Gulsoy, G., *Kinetic Parameters Influencing the Oxidation of Alloy 800H in Impure Helium at 850C.* Transactions of the American Nuclear Society, 2012. **106**: p. 1297-1300.
11. Moss, T.E., *Dynamic Strain Aging of Nickel-Base Alloys 800H and 690.* Metallurgical and Materials Transactions A, 2012. **43A**: p. 3428-3432.
12. Zinkle, S.J., *Materials Challenges in Nuclear Energy.* Acta Materialia, 2013. **61**: p. 735-758.
13. Angeliu, T.M., *Assessing the Effects of Radiation Damage on Ni-base Alloys for the Prometheus Space Reactor System.* Journal of Nuclear Materials, 2007. **336**: p. 223-237.
14. Shim, J.-H., *Modeling Precipitation Thermodynamics and Kindetics in Type 316 Austenitic Stainless Steels with Varying Composition as an Initial Step Toward Predicting Phase Stability During Irradiation.* Journal of Nuclear Materials, 2015. **462**: p. 250-257.
15. Plumtree, A., *Influence of Gamma Prime Precipitation on the Creep Strength and Ductility of an Austenitic Fe-Ni-Cr Alloy.* Metallurgical Transactions A, 1976. **7A**(1744).
16. Nanstad, R.K., *High Temperature Irradiation Effects in Selected Generation IV Structural Alloys.* Journal of Nuclear materials, 2009. **392**: p. 331-340.
17. Drabble, D.J., *A Microstructural Study of Grain Boundary Engineered Alloy 800H.* Metallurgical and Materials Transactions A, 2010. **42A**(772).
18. Tan, L., *Corrosion Behavior of Alloy 800H (Fe-21Cr-32Ni) in Supercritical Water.* Corrosion Science, 2011. **53**: p. 703-711.

19. Tan, L., *Microstructure Optimization of Austenitic Alloy 800H (Fe-21Cr-32Ni).* Materials Science and Engineering, 2011. **A 528**: p. 2755-2761.
20. Tan, L., *Microstructural Effect on Neutron Irradiation Response of Alloy 800H.* American Nuclear Society, 2012. **106**: p. 1331-1332.
21. Akhiani, H., *The Effect of Thermo-Mechanical Processing on Grain Boundary Character Distribution in Incoloy 800H/HT.* Materials Science and Engineering, 2014. **A 626**: p. 51-60.
22. Damborenea, J.d., *Improving High-Temperature Oxidation of Incoloy 800H by Laser Cladding.* Surface and Coatings Technology, 1994. **70**: p. 107-113.
23. Wang, X., *Microstructure Characterization and Dynamic Recrystallization in an Alloy 800H.* Materials Science & Engineering, 2000. **A290**: p. 180-185.
24. Nilsson, J.O., *Low Cycle Fatigue Behavior of Alloy 800H at 600C-Effect of Grain Size and Gamma Prime Precipitate Dispersion.* Fatigue of Engineering Materials and Structures, 1985. **8**(4): p. 373-384.
25. Brunger, E., *Nucleation Mechanisms of Dynamic Recrystallization in Austenitic Steel Alloy 800H.* Scripta Materialia, 1998. **38**(12): p. 1843-1849.
26. Cao, Y., *An Electron Backscattered Diffraction Study on the Dynamic Recrystallization Behavior of a Nickel-Chromium Alloy (800H) During Hot Deformation.* Materials Science and Engineering, 2013. **A 585**: p. 71-85.
27. Cao, Y., *Hot Deformation Behavior of Alloy 800H at Intermediate Temperatures: Constitutive Models and Microstructure Analysis.* Journal of Materials Engineering and Performance, 2014. **23**(12): p. 4298-4308.
28. Cao, Y., *Dynamic Behavior and Microstructural Evolution During Moderate to High Strain Rate Hot Deformation of a Fe-Ni-Cr Alloy (Alloy800H).* Journal of Nuclear Materials, 2015. **456**: p. 113-141.
29. Miodownik, N.S.a.A.P., *CALPHAD Calculation of Phase Diagrams a Comprehensive Guide*. Pergamon Materials Series, ed. R.W. Cahn. Vol. 1. 1998: Elsevier Science Inc.

APPENDIX

General Requirements			
UNS designation	N08800	N08810	N08811
INCOLOY alloys	800	800H	800HT
Nickel	30.0-35.0	30.0-35.0	30.0-35.0
Chromium	19.0-23.0	19.0-23.0	19.0-23.0
Iron	39.5 min.	39.5 min.	39.5 min.
Carbon	0.10 max.	0.05-0.10	0.06-0.10
Aluminum	0.15-0.60	0.15-0.60	0.25-0.60
Titanium	0.15-0.60	0.15-0.60	0.25-0.60
Aluminum + Titanium	0.30-1.20	0.30-1.20	0.85-1.20
ASTM grain size	Not specified	5 or coarser	5 or coarser

Note: These alloys can be specified to more restrictive compositions on a specific order basis.

INCOLOY alloy 800H, Special Requirements*	
Carbon	0.08 max.
Aluminum + Titanium	0.4-0.7
ASTM grain size	Special

*As agreed for specific orders.

Figure 24-Allying compositions for Incoloy Alloys 800, 800H, and 800HT as designated by Special Metals Corporation [4]

Density, lb/in^3	0.287
g/cm^3	7.94
Melting Range, °F	2475-2525
°C	1357-1385
Specific Heat, (32-212°F), Btu/lb•°F	0.11
(0-100°C), J/kg•°C	460
Permeability at 70°F (21°C) and 200 oersted (15.9 kA/m)	
Annealed	1.014
Hot-Rolled	1.009
Curie Temperature, °F	-175
°C	-115

Figure 25-General Properties of the Incoloy 800 series provided by Special Metals Corporation [4]

Temperature	Tensile Modulus	Shear Modulus	Poisson's Ratio[b]
°F	10^3 ksi	10^3 ksi	
-310	30.55	11.45	0.334
75	28.50	10.64	0.339
200	27.82	10.37	0.341
400	26.81	9.91	0.353
600	25.71	9.47	0.357
800	24.64	9.04	0.363
1000	23.52	8.60	0.367
1200	22.37	8.12	0.377
1400	21.06	7.58	0.389
1600	19.20	6.82	0.408
°C	GPa	GPa	Poisson's Ratio[b]
-190	210.6	78.9	0.334
20	196.5	73.4	0.339
100	191.3	71.2	0.343
200	184.8	68.5	0.349
300	178.3	66.1	0.357
400	171.6	63.0	0.362
500	165.0	60.3	0.367
600	157.7	57.4	0.373
700	150.1	54.3	0.381
800	141.3	50.7	0.394

[a]Determined by dynamic method.
[b]Calculated from moduli of elasticity.

Figure 26-Modulus data recorded by Special Metals Corporation for the Incoloy 800 series metals [4]

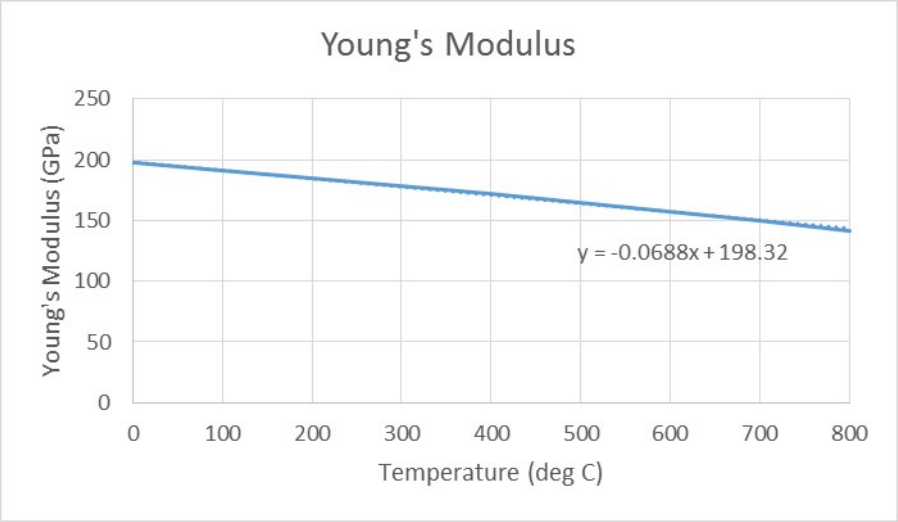

Figure 27-Calculation of temperature dependent Young's Modulus through simple graphing in Microsoft Excel from data provided by Special Metals Corporation (see Table 3)

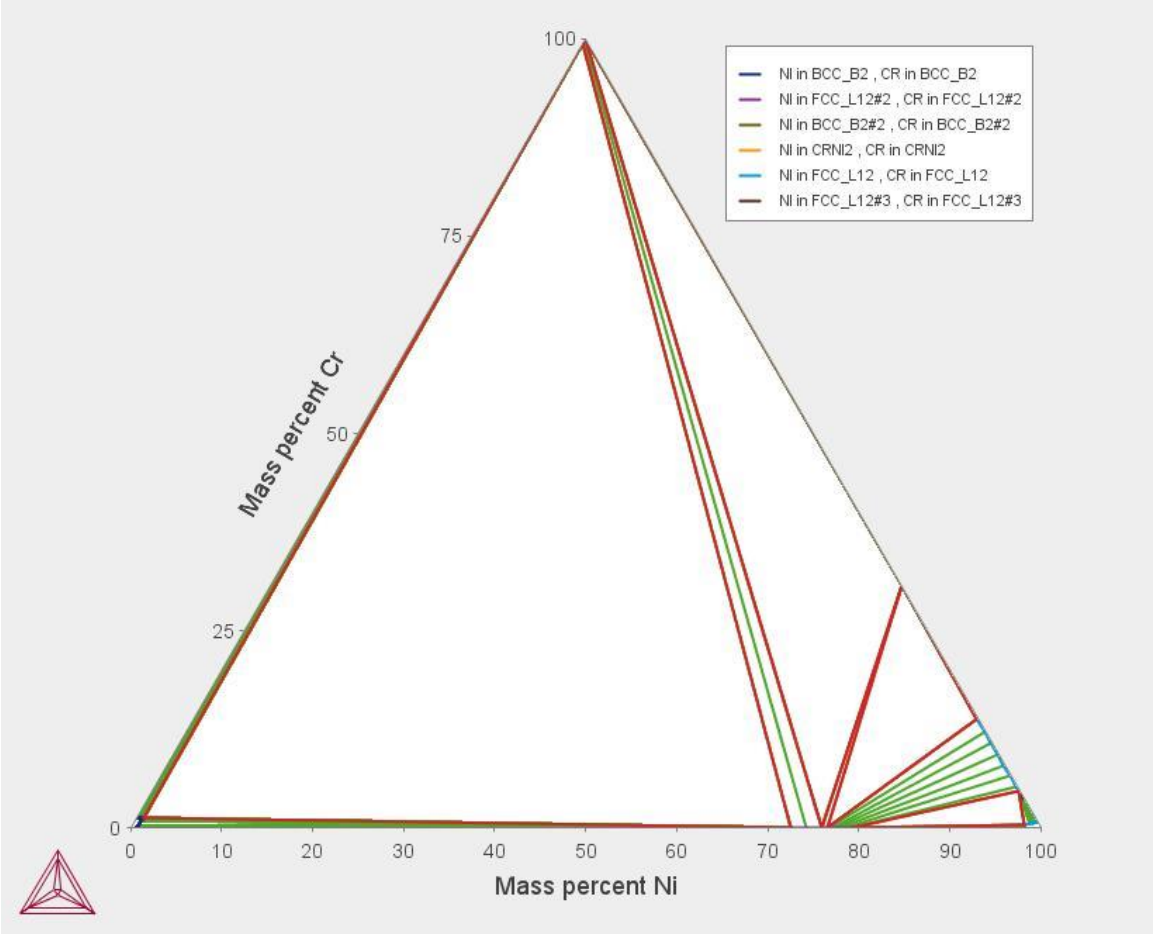

Figure 28-Ternary phase diagram calculated using ThermoCalc for the Fe-Ni-Cr system at 200˚C.

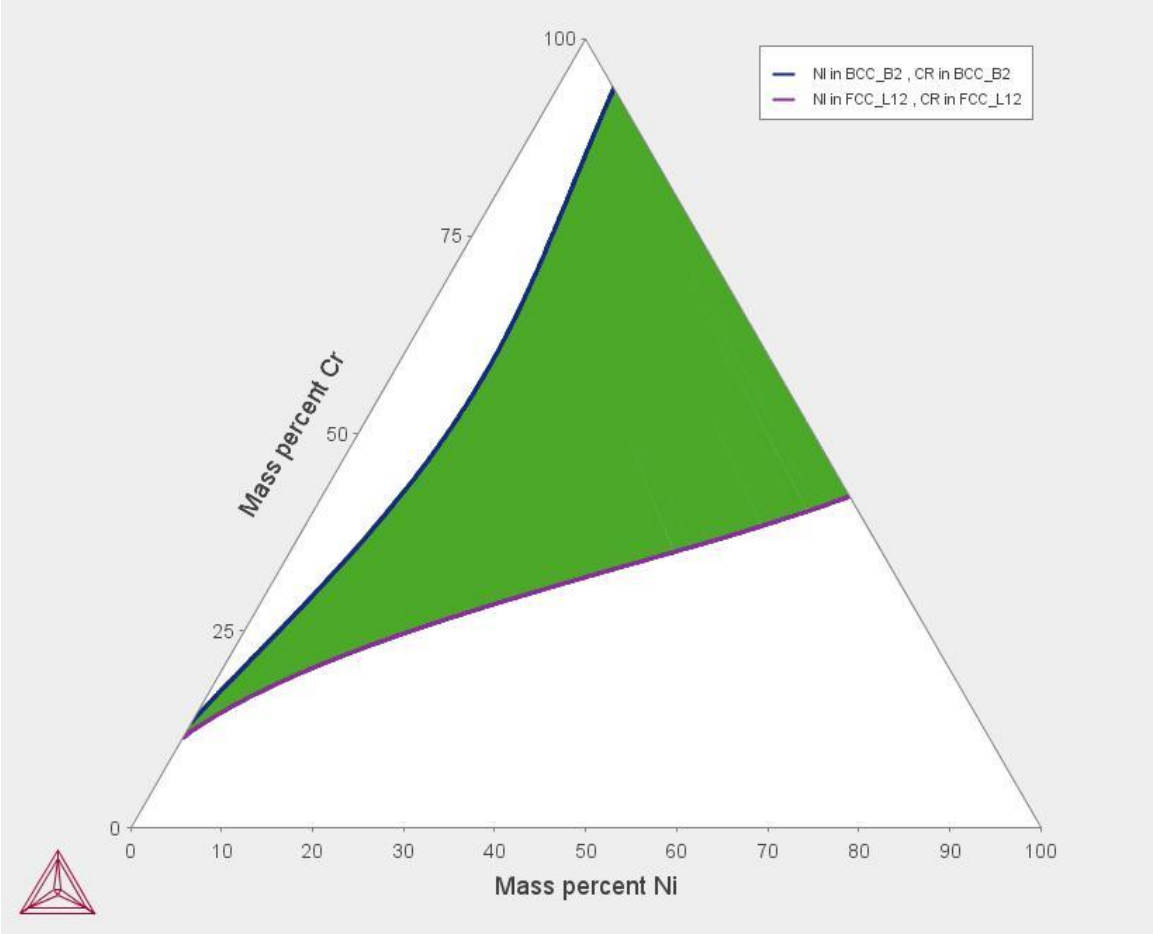

Figure 29-Ternary phase diagram calculated using ThermoCalc for the Fe-Ni-Cr system at 400˚C.

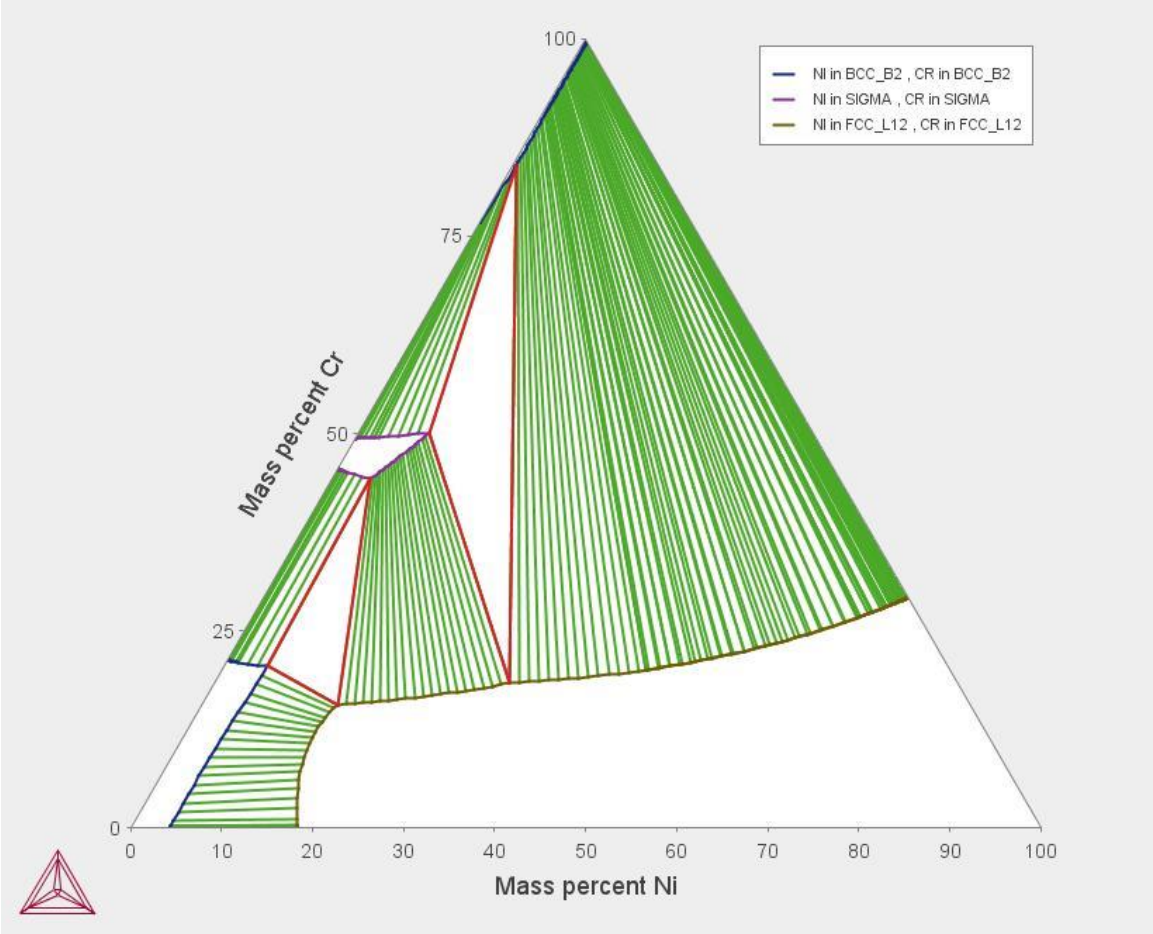

Figure 30-Ternary phase diagram calculated using ThermoCalc for the Fe-Ni-Cr system at 600˚C.

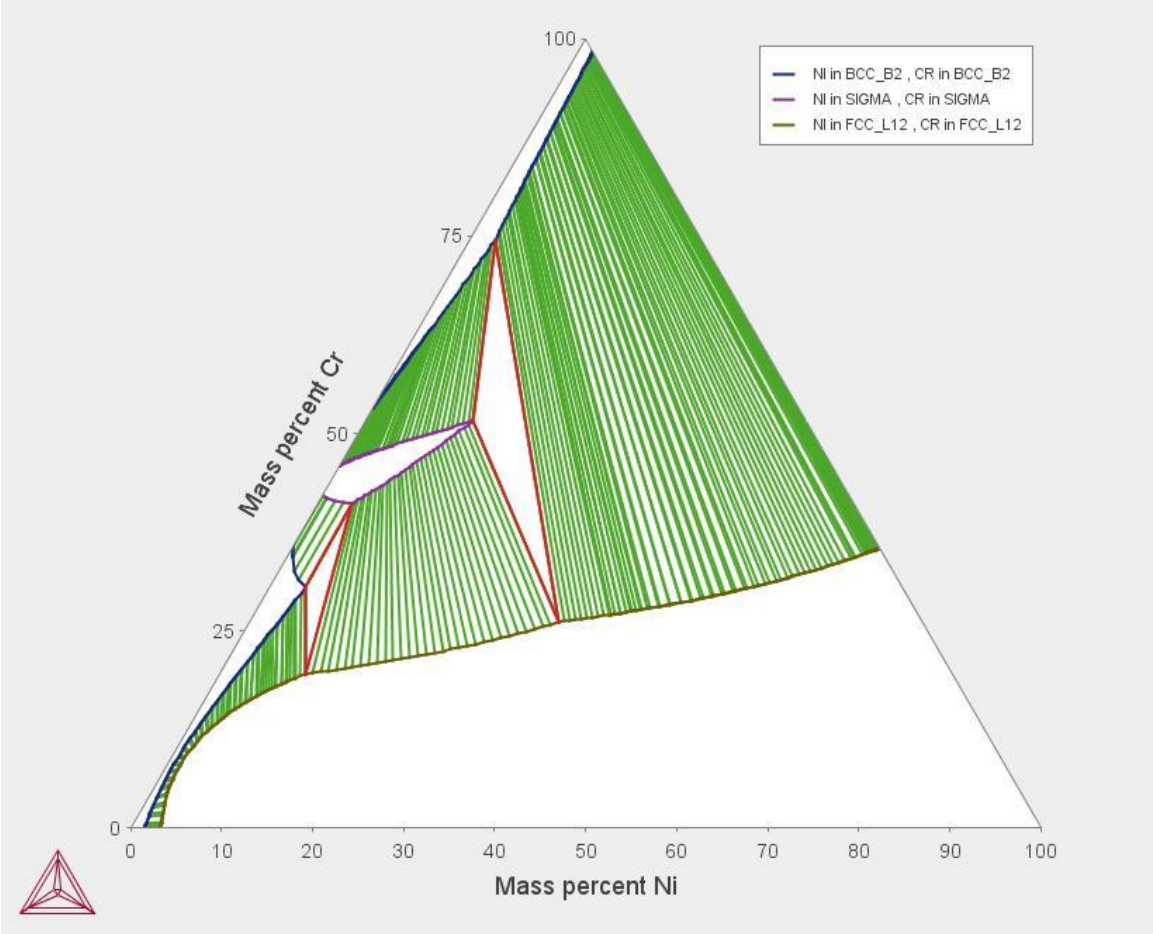

Figure 31-Ternary phase diagram calculated using ThermoCalc for the Fe-Ni-Cr system at 800˚C.

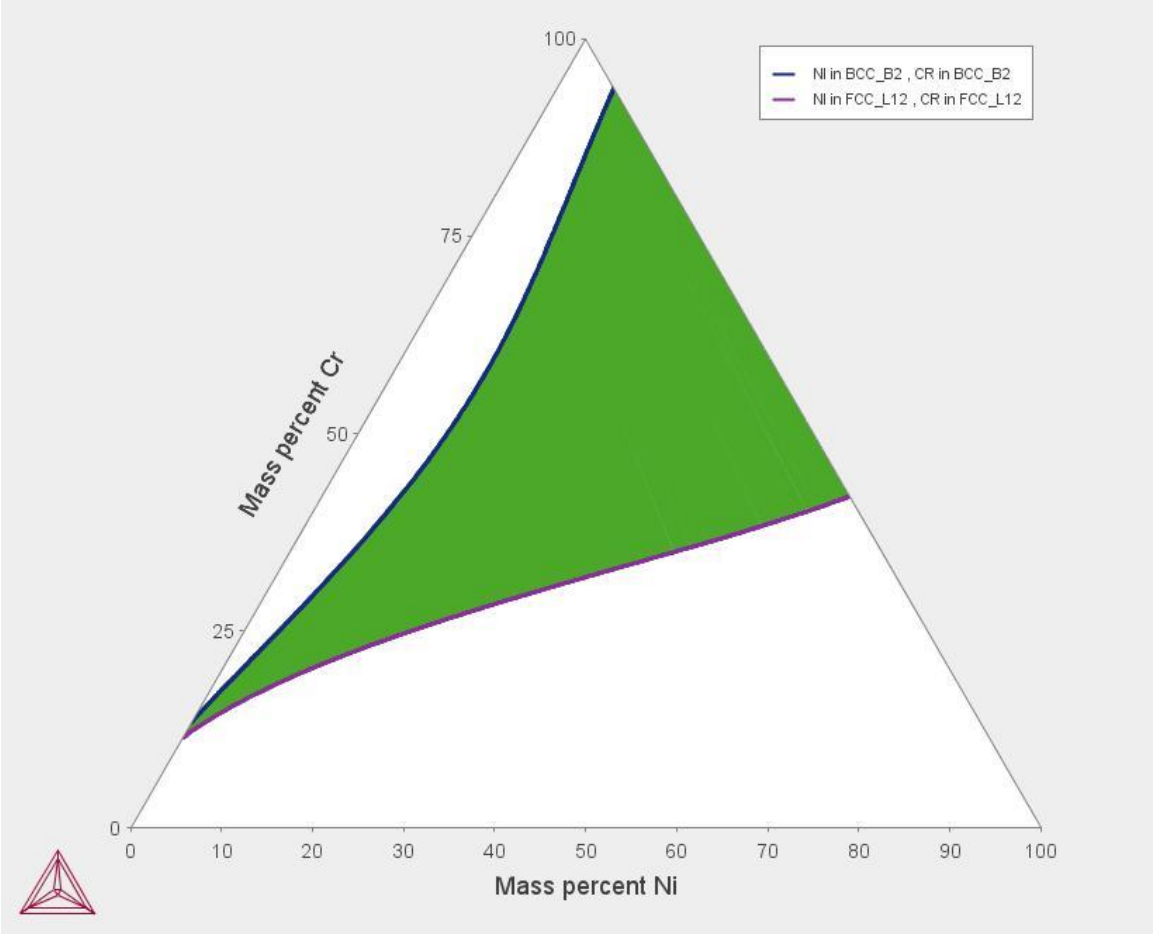

Figure 32-Ternary phase diagram calculated using ThermoCalc for the Fe-Ni-Cr system at 1000˚C.

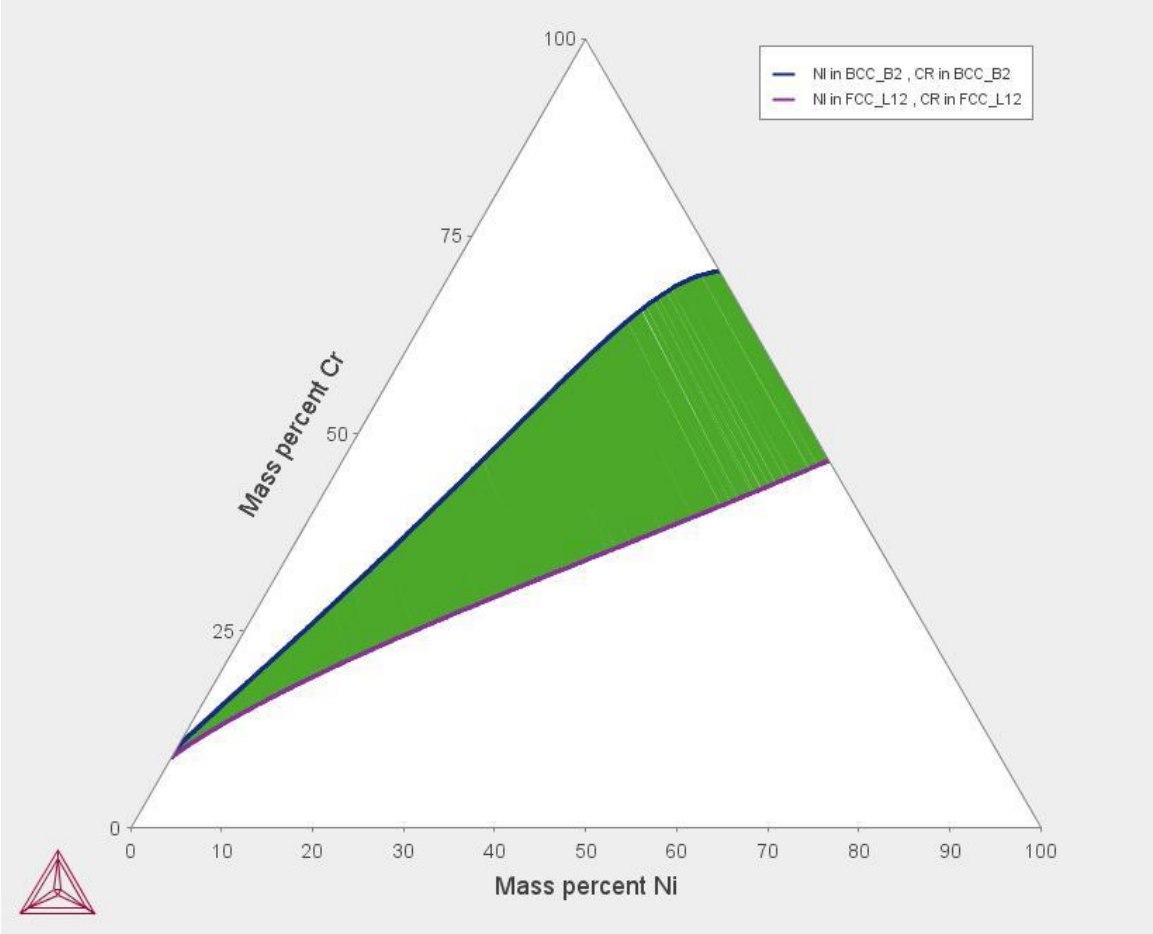

Figure 33-Ternary phase diagram calculated using ThermoCalc for the Fe-Ni-Cr system at 1200˚C.

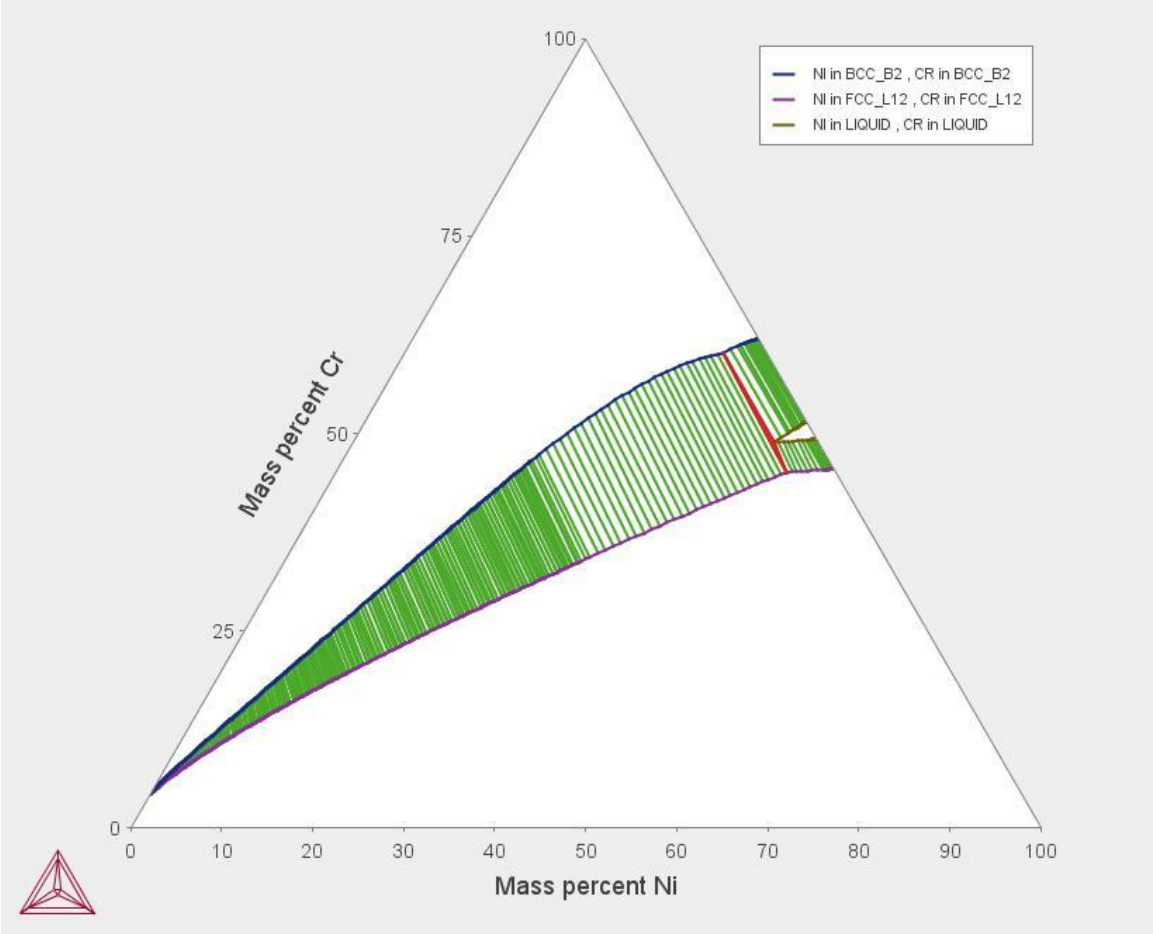

Figure 34-Ternary phase diagram calculated using ThermoCalc for the Fe-Ni-Cr system at 1350˚C.

VITA

Wayne Ethan Pratt, born in Knoxville, Tennessee to Wayne Elmer and Deborah Pratt. He graduated from Lenoir City High School in 2010 and attended the University of Tennessee, where he received a Bachelor of Science degree in Materials Science and Engineering in 2014. Ethan went on to perform his graduate studies in the Materials Sciences Department at the University of Tennessee, accepting a Graduate Research Assistant position studying long term phase stability of Alloy 800H. He will earn a Master of Science degree in Materials Science and Engineering in December of 2015.